ACS OMEGA

http://pubs.acs.org/journal/acsodf

Article

Influence of Dy^{3+} Ions on the Microstructures and Magnetic, Electrical, and Microwave Properties of $[Ni_{0.4}Cu_{0.2}Zn_{0.4}](Fe_{2-x}Dy_x)O_4$ ($0.00 \leq x \leq 0.04$) Spinel Ferrites

Munirah Abdullah Almessiere, Yassine Slimani, Hakan Güngüneş, Ayse Demir Korkmaz, Tatiana Zubar, Sergei Trukhanov, Alex Trukhanov,* Ayyar Manikandan, Fatimah Alahmari, and Abdulhadi Baykal

Cite This: *ACS Omega* 2021, 6, 10266−10280

Read Online

ACCESS | Metrics & More | Article Recommendations

ABSTRACT: $[Ni_{0.4}Cu_{0.2}Zn_{0.4}](Fe_{2-x}Dy_x)O_4$ spinel ferrite nanoparticles with different Dy^{3+} concentrations ($0.00 \leq x \leq 0.04$) were prepared by a citrate sol−gel auto-combustion technique. A strong correlation among Dy concentration, structural parameters, and magnetic, electrical, and microwave properties was established. An increase in the Dy^{3+} concentration is the reason for a rise in the crystal structure parameters (due to different ionic radii of Fe and Dy ions) and a slight increase in the average particle size with a minor reduction in the specific surface area. It was observed that Dy^{3+} ions prefer to occupy the octahedral B site due to their large ionic radius (0.91 Å). The explanation of the electrical and magnetic properties was given in terms of the features of $Dy^{3+}-O^{2-}-Fe^{3+}$ dysprosium−oxygen−iron indirect exchange. The occurrence of the intensive changes in amplitude−frequency characteristics was observed from 1.6 to 2.7 GHz. The explanation of electromagnetic absorption was given in terms of the peculiarities of the microstructure (resonance of domain boundaries). The results open perspectives in the utilization of $[Ni_{0.4}Cu_{0.2}Zn_{0.4}](Fe_{2-x}Dy_x)O_4$ spinel ferrite nanoparticles as functional materials for targeted drug delivery and hyperthermia applications.

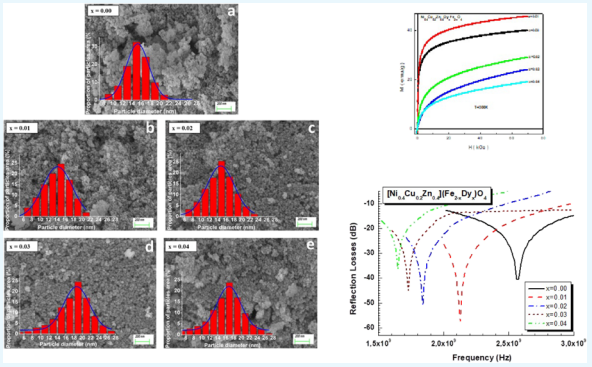

1. INTRODUCTION

A large number of papers demonstrate intensive investigations of the synthesis and physical properties of the complex oxides based on transition metal ions[1,2] which indicate the fundamental significance and practical importance of the complex oxides. The fundamental significance of such oxides is based on the strong coupling among chemical composition, structural parameters, and physical properties. Their practical importance is established by the applications of these materials in various areas. Therefore, we can state that ferrites are the most promising compounds among the complex magnetic oxides from this point of view.[3−5] Ferrites are complex iron oxides with different crystal structures. Currently, a variety of different ferrite types exists—spinels, hexagonal ferrites, garnets, and orthoferrites. The general formula of spinels is AB_2O_4 (where A is a divalent cation and B is a Fe^{3+} ion or another substituent with an equivalent charge).[6] Spinel ferrites are most frequently used ferrites due to many reasons. The magnetic and electrical properties of spinels greatly depend on the composition (level of iron substitution, oxygen stoichiometry, and charge ordering) and structural parameters. Spinel ferrites are promising compounds that can be used in the manufacture of heating inductors in catalytic chemical reactors because of their high Curie temperatures and moderate magnetic losses in the kHz range.[7,8] In addition, they can be used as magnetic catalysts that facilitate separation.[9] The use of ferrites for microwave heating and magnetic separation in chemical reactors provides a new technological platform for system integration.[10] In such systems, magnetic particles embedded in composite catalytic microparticles are used as microwave heating receivers,[11,12] and heating provides an efficient and uniform heat transfer to the flowing liquid.[13] Recently, the rapid growth of microwave devices requires more detailed research on the promising functional compounds for high-frequency applications. Spinels with nanosized grains demonstrate an enhancement of the characteristics in comparison with the bulk analogues. The grain boundaries are an important factor in the charge transport in nanoferrites

Received: February 2, 2021
Accepted: March 26, 2021
Published: April 8, 2021

in contrast to their bulk counterparts. Quasi-one-dimensional structures based on spinels are used in catalysis[14−16] and for battery applications.[17,18]

Nickel−zinc ferrites attract great attention of researchers due to their properties such as high electrical resistivity, high magnetic permeability, high Curie temperature, low power loss, and so forth.[19] Nickel ($NiFe_2O_4$) and zinc ($ZnFe_2O_4$) ferrites have found technological applications as gas sensors,[20,21] catalysts,[22−24] microwave devices,[25] photoelectrochemical cells,[26] and photochemical hydrogen production.[27,28] They are also used as cores, radio frequency circuits, absorbers of electromagnetic waves,[29,30] and in medicine.[31] Many authors have attempted to modify the properties of Ni−Zn spinels by substitution with other elements in A-sites. For example, $Ni_{0.49}Zn_{0.49}Co_{0.02}Fe_2O_4$-nanosized ferrites were prepared by a citrate precursor method by P. Mathur et al.[32] It was established that the material shows almost a constant complex permeability and permittivity in the frequency range from 10 to 200 MHz, equal to ∼9.1 + j0.51 (loss tangent ∼ 0.05) and ∼4.4 + j0.16 (loss tangent ∼ 0.036), respectively. There are many articles reporting the preparation of Ni−Cu−Zn ferrites with nanosizes as well as bulk materials. For example, Roy et al. synthesized $(Ni_{0.25-x}\ Mg_xCu_{0.20}Zn_{0.55})$-$Fe_2O_4$ ferrite nanoparticles with crystallite sizes between 19 and 22 nm by a sol−gel auto-combustion approach. As the substitution of Ni by Mg increased, a decline in magnetic loss was observed while the AC resistivity and permeability increased. In another study by Chakrabarti et al., a chemical route technique was employed to obtain $Ni_{0.2}Zn_{0.6}Cu_{0.2}Fe_2O_4$ nanocrystals, and they stated that below 80 K, the nanoparticles exhibited superparamagnetism and their saturation magnetization (Ms) raised as the particle size increased.[33] Batoo and co-workers investigated the effect of Zn doping on nano-sized $Ni_{0.7-x}Cu_{0.3}Fe_2O_4$ ferrites by auto-combustion. It has been found that when the applied field frequency was increased, a decrease in loss tangent and dielectric constant was detected.[34] Reddy and co-workers chose a microwave sintering technique. As the substitution of Zn with Ni increased, DC resistivity diminished, while Ms, permeability, dielectric loss, and dielectric constant enhanced.[35] Some studies have found that setting up the amount of copper ions as Cu^{2+} = 0.2 can result in obtaining good electrical resistivity and Ms. In addition, when the molar ratios of nickel and zinc are equal, the highest Ms values can be attained.

A number of research studies were investigated on the synthesis of $Ni_{0.4}Cu_{0.2}Zn_{0.4}Fe_2O_4$ ferrites by different methods for the substitution of Fe^{3+} ions as well as other metallic ions for varying the electrical and magnetic properties of the spinel ferrites. For instance, a reverse micelle process was employed by Ghasemi et al. to synthesize $Ni_{0.6-x}Cu_xZn_{0.4}Fe_2O_4$ $(0 \le x \le 0.5)$ nano-sized ferrites. The increase in copper resulted in a rise in the saturation magnetization of ferrites.[36] Jacobo and Bercoff[37] studied the structure and electromagnetic properties of Y^{3+}-substituted Ni−Zn spinels prepared by a sol−gel method. Y^{3+} substitution slightly reduces the average crystallite size and unit cell parameters, and it modifies the saturation magnetization, permeability, and permittivity. The dielectric constant decreases with the Y content, showing a constant behavior in the explored frequency range. In another study, Liu et al.[38] explored the doping effect of Sm^{3+} on the magnetic and dielectric properties of Ni−Zn spinels. $Ni_{0.5}Zn_{0.5}Sm_xFe_{2-x}O_4$ samples were prepared by a conventional two-step solid sintering method. It was found that the substitution by the Sm^{3+} cations decreased the dielectric loss in the frequency range of 1−100 MHz, but the dielectric loss increased in the frequency range of 100−1000 MHz. At x = 0.05, the dielectric loss reached the lowest value. Qian and co-workers[39] investigated the influence of Nd^{3+} substitution for Ni−Zn spinels and established the improvement of microwave absorption. Nanocrystalline $Ni_{0.5}Zn_{0.5}Nd_xFe_{2-x}O_4$ ferrites were synthesized by a sol−gel route combined with a self-propagating combustion method. The Nd^{3+} substitution increased the polarization relaxation and polarization intensity of the material and promoted the enhancement of microwave absorption capacity. At x = 0.04, the optimal absorption peak reaches −20.8 dB at 4.4 GHz with a sample thickness of 8.5 mm and an effective absorption bandwidth of 3.2 GHz at R_L (reflection losses) < −10 dB. Eltabey and co-workers studied the structural and dielectric properties of $Ni_{0.4}Cu_{0.2}Zn_{0.4}Al_xFe_{2-x}O_4$ (x = 0 to x = 0.15) ferrites synthesized by conventional solid-state reactions. As the content of Al increased, the crystallite size decreased and the substitution of iron ion with aluminum ion caused an enhancement in the initial permeability and DC resistivity.[40] Finally, an ultrasound-assisted chemical technique was developed to prepare Ni−Zn−Cu spinels by Harzali et al.[41] The ultrasound-assisted technique, which is also known as the sonochemical method, has various advantages compared to other techniques. In addition to being an environmentally friendly approach, the reduced reaction time and a minimum cost with energy are factors influencing the sonochemical method as an attractive technique for synthesis.

Rare-earth substitution of ferrites can dramatically change their electric, magnetic, and microwave properties. The difference in the ionic radii of the ferrite ion and the rare-earth ion can result in microstrain causing the deformation of the spinel structure. R Tholkappiyan and K Vishista in ref 42 demonstrated a strong correlation of the La^{3+} substitution and optomagnetic properties of the Zn ferrite nanoparticles. The 4f electrons of trivalent rare-earth metal ions in which strong spin−orbit angular momentum coupling is present are shielded by $5s^25p^6$ subshells, and hence, the surrounding ions' electric potential remains inert to the 4f electrons.[43] This results in an enhancement in the electromagnetic properties. There are a number of studies investigating the rare-earth substitution effect in spinel ferrites. Harzali et al. prepared nickel copper zinc ferrites substituted with Eu^{3+}, Sm^{3+}, Gd^{3+}, and Pr^{3+} by ultrasound irradiation. They found that the Pr^{3+} doping enhanced the value of Ms at room temperature, considering that Pr^{3+} has a much larger ionic radius compared to Fe^{3+} while Eu^{3+} or Gd^{3+} substitution decreased the Ms values. In general, the Ms value at room temperature increases as the ionic radius of the rare-earth ion increases.[44] Kulal et al. synthesized $Co_{0.50}Zn_{0.50}Fe_{2-x}Dy_xO_4$ ferrite particles and found that as the value of "x" increased, the lattice constant decreased, the crystallite size increased, and the porosity increased.[42]

In the present paper, to the best of our knowledge, there is no report that has investigated the alteration of Dy^{3+} ion concentration on the structural parameters and magnetic, electrical, and microwave properties of the $[Ni_{0.4}Cu_{0.2}Zn_{0.4}]$-$(Fe_{2-x}Dy_x)O_4$ $(0.00 \le x \le 0.04)$ spinel ferrite nanoparticles (SFNPs) produced though the citrate sol−gel auto-combustion method.

https://doi.org/10.1021/acsomega.1c00611
ACS Omega 2021, 6, 10266−10280

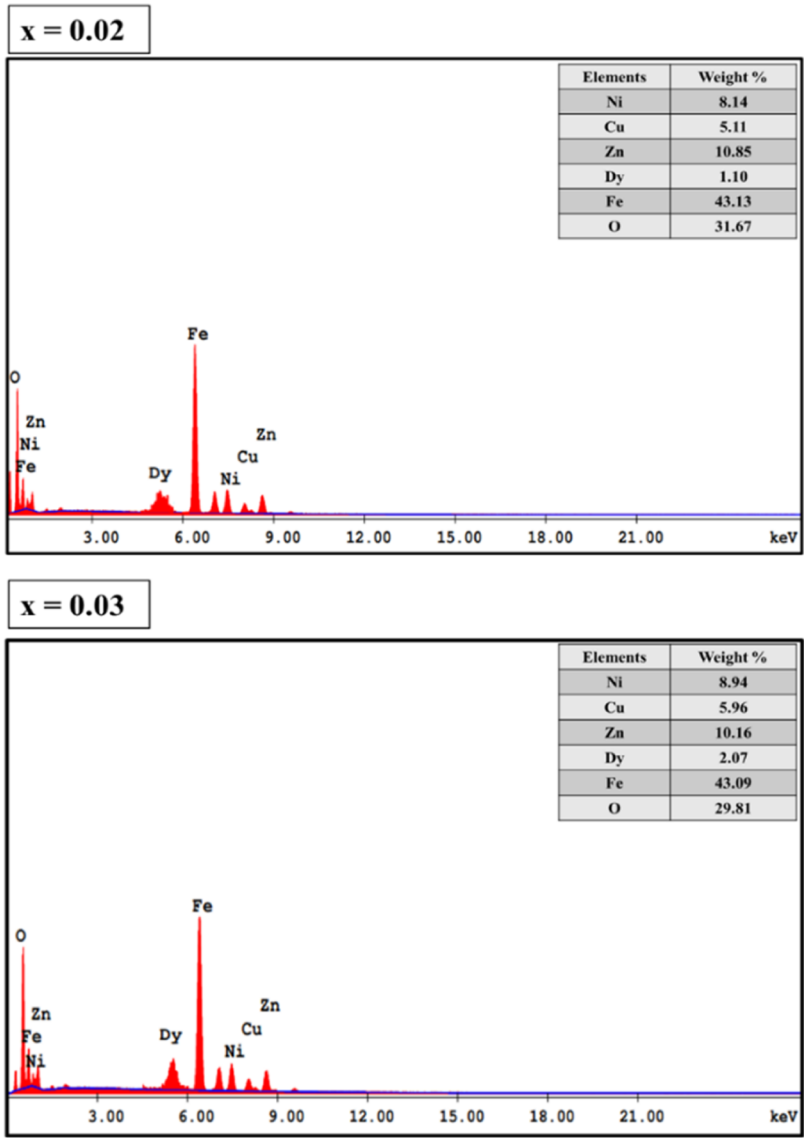

Figure 1. EDX of $[Ni_{0.4}Cu_{0.2}Zn_{0.4}](Fe_{2-x}Dy_x)O_4$ SFNPs (x = 0.02 and 0.03).

2. RESULTS AND DISCUSSION

2.1. Structural Parameters. The elemental weight percentage of $[Ni_{0.4}Cu_{0.2}Zn_{0.4}](Fe_{2-x}Dy_x)O_4$ SFNPs (x = 0.02 and 0.03 and) was estimated using EDX as shown in Figure 1. The EDX spectra of all samples have confirmed the occurrence of Ni, Cu, Zn, Dy, Fe, and O, which referred to the efficiency of the synthesis method.

The crystal structure parameters were investigated using X-ray diffraction (XRD). A high accuracy was achieved by better statistics (obtained by a longer holding time) and using FullProf software (Rietveld refinement). The XRD patterns for $[Ni_{0.4}Cu_{0.2}Zn_{0.4}](Fe_{2-x}Dy_x)O_4$ where $0.00 \leq x \leq 0.04$ are shown Figure 2 (see the inset).

The single phase and homogeneity (without any impurities) of all the investigated samples were identified after analyzing the XRD results. The cubic space group $Fd\bar{3}m$ (no. 227) accurately describes the crystal structure of $[Ni_{0.4}Cu_{0.2}Zn_{0.4}](Fe_{2-x}Dy_x)O_4$ ($0.00 \leq x \leq 0.04$) with the standard JCPDS card no. 08-0234. There are no additional peaks in the XRD patterns. The concentration dependencies of the lattice parameter (left scale) and V, unit cell volume, (right scale) with an increase in the degree of substitution are shown in Figure 2.

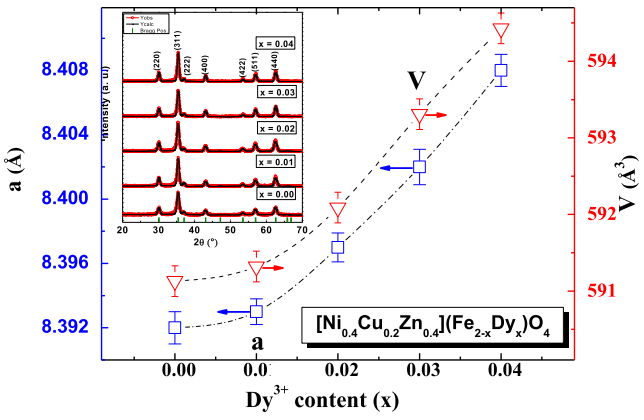

Figure 2. Concentration dependencies of the lattice parameter a (left scale) and volume V (right scale) of the $[Ni_{0.4}Cu_{0.2}Zn_{0.4}](Fe_{2-x}Dy_x)O_4$ ($0.00 \leq x \leq 0.04$) SFNP unit cell (the insets demonstrate the XRD patterns with Rietveld refinement for all samples).

https://doi.org/10.1021/acsomega.1c00611
ACS Omega 2021, 6, 10266−10280

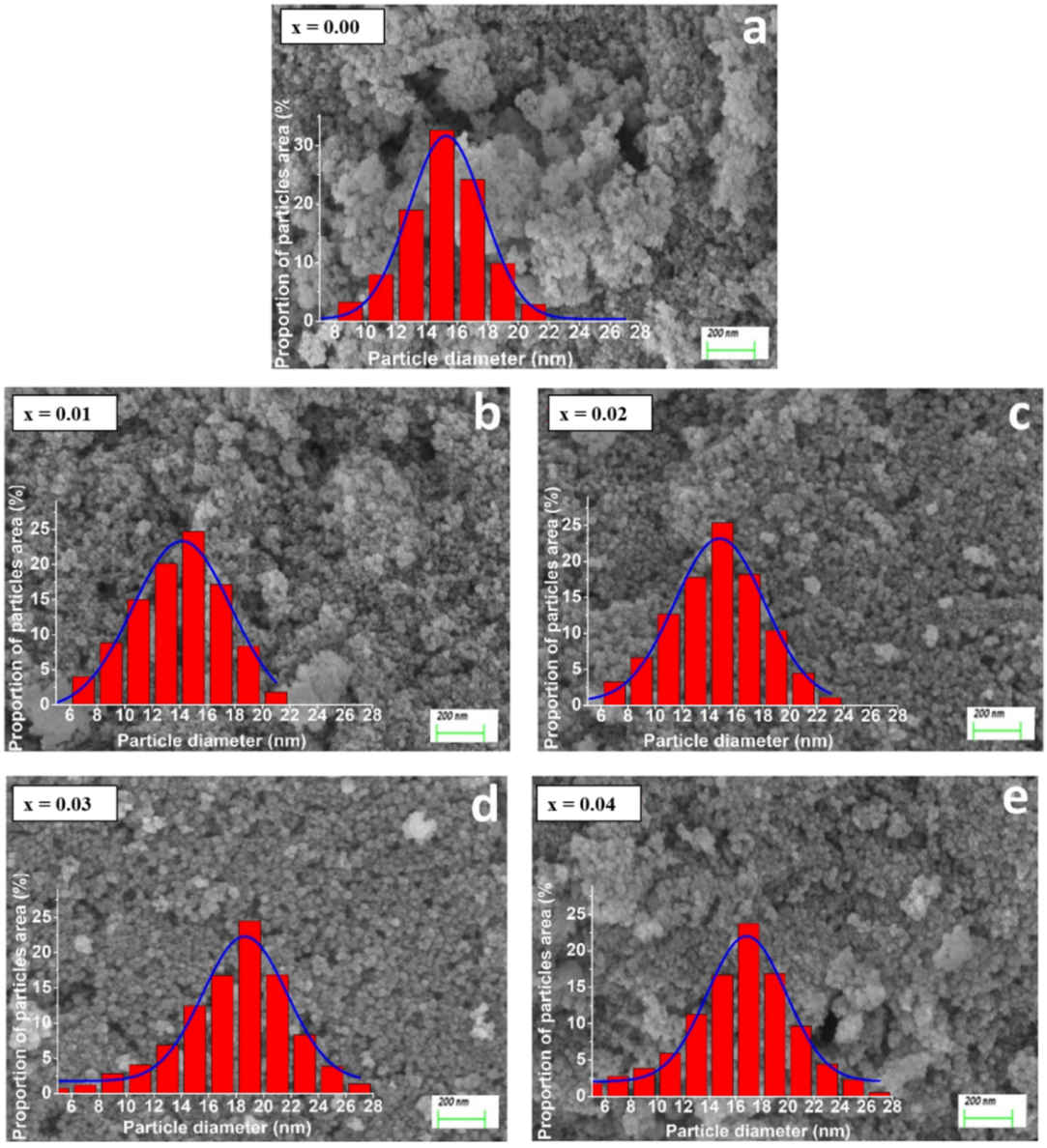

Figure 3. SEM images and histograms of the size distribution of $[Ni_{0.4}Cu_{0.2}Zn_{0.4}](Fe_{2-x}Dy_x)O_4$ SFNPs with (a) $x = 0.00$, (b) $x = 0.01$, (c) $x = 0.02$, (d) $x = 0.03$, and (e) $x = 0.04$.

The XRD investigation results indicate that the high Dy^{3+} ion concentration promotes the expansion of the lattice as evidenced by an increase in the unit cell parameter. Thus, a change in the dysprosium ion concentration from $x = 0.00$ to $x = 0.04$ causes an increase in the lattice parameter from 8.392 ± 0.006 to 8.408 ± 0.007 Å and the volume from 591.13 ± 0.04 to 594.43 ± 0.03 Å^3, respectively. The reason for this change is that the ionic radius of dysprosium is much larger than the ionic radius of iron ($R_{Dy^{3+}} = 0.091$ nm and $R_{Fe^{3+}} = 0.064$ nm for coordination number CN = 6) as discussed in ref 43. Using XRD data, the value of the average crystallite size (D_{XRD}) was calculated. A monotonic decrease in the D_{XRD} value from 19.2 to 10.8 nm was observed with an increase in the Dy concentration from $x = 0.00$ to $x = 0.04$, respectively. A decrease in D_{XRD} with an increase in the concentration of Dy^{3+} is probably associated with the hindered growth of crystallites. Dysprosium ions have a significantly larger size and are local defects that prevent the coarsening of crystallites during the synthesis.[3,43]

The scanning electron microscopy (SEM) images of $[Ni_{0.4}Cu_{0.2}Zn_{0.4}](Fe_{2-x}Dy_x)O_4$ ($x = 0.00$–0.04) SFNPs are displayed in Figure 3. The images exhibit the agglomeration of spherical particles with an average particle size (APS) of around 20 nm. Figure 2 shows the particle size distributions obtained by statistical analyses of the SEM images and their histograms. The size distribution is obtained from the SEM images by calculating the proportion of grain area with the following equation[43]

$$P_i = 0.25\frac{d_i^2 \pi n_i}{S} \quad (1)$$

where d_i is the size (equivalent disk diameter) of a given particle, S is the full area of all particles on the image, and n_i is the number of particles with a given size.[44−49] The APSs of the $[Ni_{0.4}Cu_{0.2}Zn_{0.4}](Fe_{2-x}Dy_x)O_4$ ($x = 0.00$–0.04) SFNPs were specified by the maxima of the Gaussian function recitation the size distribution plots. The graphs of particle size distributions (stereological analysis data) were added to the SEM images.

https://doi.org/10.1021/acsomega.1c00611
ACS Omega 2021, 6, 10266−10280

An analysis of the results showed that the samples have very close particle size. This also applies to the dispersion of particles of each sample and the APS of the nanosized spinel ferrites with x = 0.00−0.04. The characteristic Gaussian function describing the size distribution helps to determine the exact value of the most common size of practices in each sample as the Gaussian maximum positions.

The average size of the particle is presented in Figure 4 (black line). It has been found that the APS was 15 nm for

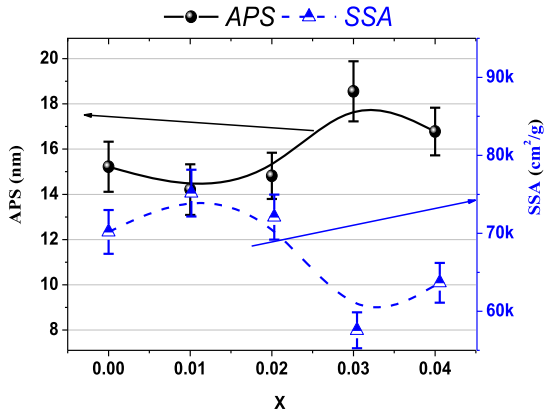

Figure 4. APS (left scale) and specific surface area or SSA (right scale) for $[Ni_{0.4}Cu_{0.2}Zn_{0.4}](Fe_{2-x}Dy_x)O_4$ ($0.00 \le x \le 0.04$) SFNPs.

$[Ni_{0.4}Cu_{0.2}Zn_{0.4}](Fe_{2-x}Dy_x)O_4$ (x = 0.00−0.04) SFNPs. The nanospinel ferrites with x = 0.01 and 0.02 have the minimum APS values but differ from the initial sample (x = 0.00) in a large dispersion. Therefore, the particles size of the x = 0.00 sample varies from 8 to 22 nm and the x = 0.01 and x = 0.02 samples from 6 to 24 nm.

The largest dispersion widths vary between 4 and 28 nm in samples with x = 0.03 and x = 0.04. In general, the APS tends to increase nonlinearly with increasing dysprosium concentration. However, it exhibits the biggest size (19 nm) at x = 0.03 and slightly decreases to 17 nm at x = 0.04. The value of the SSA of the investigated samples was calculated from[43]

$$\mathrm{SSA} = \frac{(p_1 \cdot S_1 + p_2 \cdot S_2 \ldots + p_n \cdot S_n)}{100\%} \quad (2)$$

where p_i is the content of the fraction (%) obtained by the results of size distribution, n is the number of fraction, and S_i refers to the surface area of particles of a given fraction, which was calculated as[43]

$$S_i = \frac{6}{\rho \cdot d_i} \quad (3)$$

The density (ρ) of the -SFNPs was taken equal to 5.6×10^3 kg/m^3. The particle shape was considered spherical to simplify SSA calculations. The calculation results are given in Figure 3 (right scale). The SSA is closely related to particle size and inversely proportional to APS. The SSA of the nanosized spinel ferrites is about 70 000 ± 500 cm^2/g. Then, the SSA nonlinearly decreases (simultaneously with the increase of the particle size) with the increase of the concentration of Dy. The largest particle size that corresponds to the sample where x = 0.03 provides the minimum surface area (56,000 ± 700 cm^2/g).

2.2. Magnetic Structure and Magnetic Properties.

The room-temperature Mössbauer spectra of $[Ni_{0.4}Cu_{0.2}Zn_{0.4}](Fe_{2-x}Dy_x)O_4$ (x = 0.00−0.04) SFNPs are depicted in Figure 5. Various Mössbauer parameters are calculated and given in Table 1.

At x = 0.04, a paramagnetic doublet as well as ferromagnetic sextets formed. The area of this doublet is 9.4601% for x = 004. The largest hyperfine field and the smaller isomer shift values reveal the presence of Fe^{3+} ions in the tetrahedral A site, while the other sextet having a smaller hyperfine field indicates the existence of Fe^{3+} ions in the octahedral B site.[49] The reason for the higher value of the A site hyperfine field than that of the B site is attributable to the less covalent nature of the Fe^{3+}−O^{2-} bond.[50] The values of the I.S of the magnetic patterns (A and B) range between 0.261 and 0.344 mm/s at room temperature. These values are associated with the characteristics of the high spin Fe^{3+} charge state.[51] It can be deduced from the increment in the isomer shift of the B site that the s electron density of Fe^{3+} ions at this site decreases with substitution. At the same

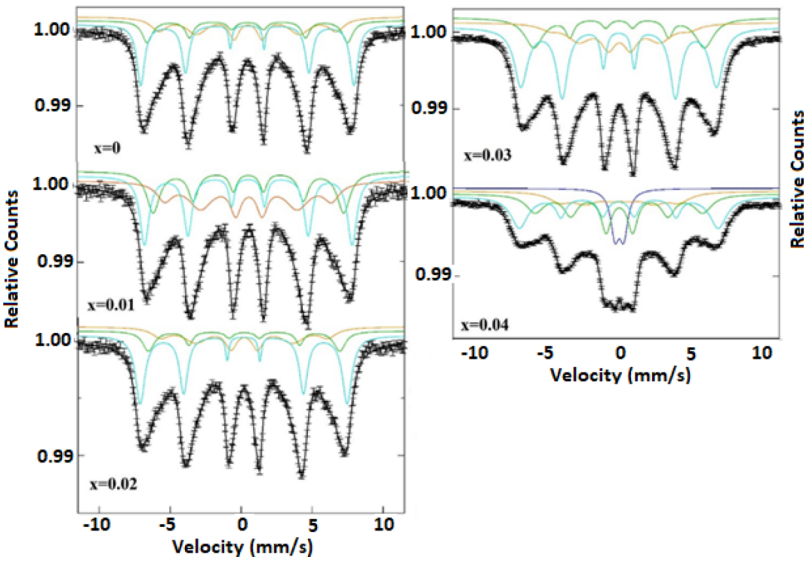

Figure 5. Room-Temperature Mössbauer spectra of $[Ni_{0.4}Cu_{0.2}Zn_{0.4}](Fe_{2-x}Dy_x)O_4$ ($0.00 \le x \le 0.04$) SFNPs.

https://doi.org/10.1021/acsomega.1c00611
ACS Omega 2021, 6, 10266−10280

Table 1. Parameters of Mössbauer Spectra of $[Ni_{0.4}Cu_{0.2}Zn_{0.4}](Fe_{2-x}Dy_x)O_4$ ($0.00 \le x \le 0.04$) SFNPs (H_{hf}: Hyperfine Magnetic Field; I.S: Isomer Shift; Q.S: Quadrupole Splitting; and Area: Relative Area)[a]

X	spectral component	I.S. (±0.01) (mm s^{-1})	Q.S. (±0.02) (mm s^{-1})	H_{hf} (±0.1) (T)	area (%)
0.00	Sx-A: Fe^{+3}	0.277	0.013	45.212	19.489
	Sx-B_1: Fe^{+3}	0.291	−0.09	42.486	25.434
	Sx-B_2: Fe^{+3}	0.318	−0.027	37.616	55.077
0.01	Sx-A: Fe^{+3}	0.289	0.024	44.177	19.919
	Sx-B_1: Fe^{+3}	0.305	0.01	40.829	29.18
	Sx-B_2: Fe^{+3}	0.315	−0.052	35.776	50.901
0.02	Sx-A: Fe^{+3}	0.277	0.005	45.207	24.88
	Sx-B_1: Fe^{+3}	0.318	−0.019	41.777	19.804
	Sx-B_2: Fe^{+3}	0.321	−0.033	36.527	55.316
0.03	Sx-A: Fe^{+3}	0.29	−0.007	42.757	35.078
	Sx-B_1: Fe^{+3}	0.319	−0.004	37.275	22.349
	Sx-B_2: Fe^{+3}	0.344	0.012	30.497	42.573
0.04	Sx-A: Fe^{+3}	0.282	0.02	43.458	24.748
	Sx-B: Fe^{+3}	0.318	−0.027	36.647	28.412
	Sx-B_2: Fe^{+3}	0.341	−0.009	25.894	37.381
	Db: Fe^{+3}	0.328	0.617		9.4601

[a]Three ferromagnetic sextets have been applied to fit the spectrum, A for the tetrahedral sites and B_1 and B_2 for the octahedral positions for samples.

time, the isomer shift of the A site fluctuates with an increase of substituent ions. The chemical disorder in the material leads to the occurrence of quadrupole splitting (Q.S) that culminates in an electric field gradient.[52] We can also gain some important knowledge about the crystal lattice symmetry and its local distortions by utilizing the Q.S values. The small Q.S values of components can be negligible. This reveals the fact that the substituted ions do not influence the cubic symmetry of oxygen ions around Fe^{3+} in the cubic ferrite structure. The relative area of A site increases with an increase in Dy^{3+} concentration up to x = 0.03. Then, the superparamagnetic doublet composes in the sample. The area of these sextets and the doublet is directly proportional to the number of Fe^{3+} ions in the corresponding sites. Above x = 0.03, the relative area of the A site decreases but that of the B site almost does not change. It is well known that the octahedral sites are generally occupied by ions, whereas the tetrahedral sites are preferred by small size ions. Rare-earth ions generally locate at the octahedral B site owing to the large ionic radius.[53,54] These show that the larger ions of Dy^{3+}(0.91 Å) prefer to occupy the octahedral B site.[42] Above x = 0.03, some of Fe^{3+} ions at the A site exhibit superparamagnetic properties. At the same time, the hyperfine field of A and B sites decreases with the increase of doped ions. The displacement Dy^{3+} ions by Fe^{3+} ions on B sites leads to a decrease of the magnetic moment on the B site. This shows that $Fe_A^{3+}-O^{2-}-Fe_B^{3+}$ interactions weaken. Therefore, the hyperfine magnetic field of A and B sites decreases with substitutions.

The field dependence of magnetization for the $[Ni_{0.4}Cu_{0.2}Zn_{0.4}](Fe_{2-x}Dy_x)O_4$ (x = 0.00−0.04) SFNPs at room temperature is shown in Figure 6.

It is well known that the microwave properties of magnetodielectrics largely determine the magnetic parameters such as spontaneous magnetization and coercive force.[54] These parameters can be controlled by substituting various cations

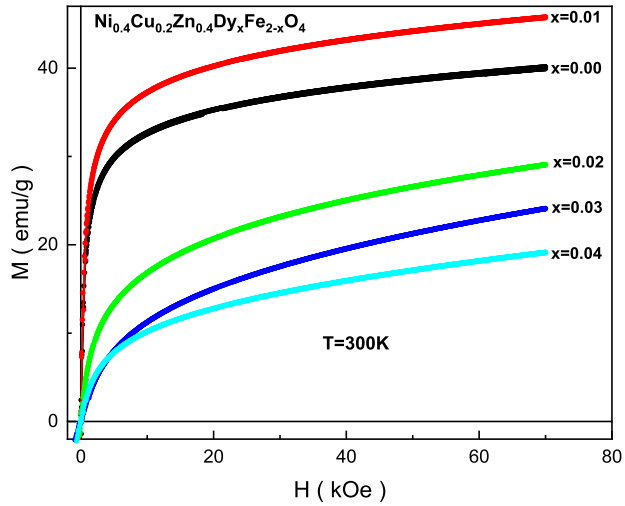

Figure 6. Field dependence of magnetization for the $[Ni_{0.4}Cu_{0.2}Zn_{0.4}](Fe_{2-x}Dy_x)O_4$ ($0.00 \le x \le 0.04$) SFNPs at T = 300 K.

in different contents and synthesis methods.[55,56] In this work, the Dy^{3+} dysprosium cations as the substituting cations were selected. The Dy^{3+} dysprosium cation in octahedral coordination has an ionic radius of ∼0.091 nm. This is almost twice the ionic radius of the Fe^{3+} iron cation ∼0.064 nm in the same anionic surrounding. This type of substitution causes a significant increase in the unit cell. The increasing $Fe^{3+}(Dy^{3+})-O^{2-}$ bond lengths and the $Fe^{3+}-O^{2-}-Dy^{3+}$ bond angles are expected to weaken the exchange interaction in the $Fe^{3+}(Dy^{3+})-O^{2-}-Dy^{3+}(Fe^{3+})$ dysprosium−oxygen−iron chains. Numerous distorted chemical bonds on the surface of nanoparticles will also contribute to the weakening of the exchange interactions. As can be seen from Figure 6, the magnetization naturally decreases with increasing Dy^{3+} dysprosium cation substitution, except for the sample with x = 0.01. The magnetization value for the sample with x = 0.00 at room temperature in a field of 70 kOe is ∼40 emu/g. The maximum magnetization value of ∼46 emu/g under these conditions is observed for x = 0.01, while the minimum value of ∼19 emu/g is observed for x = 0.04. The difference between the maximum and minimum value is ∼59%. The coercive force decreases from ∼56 Oe for x = 0.00 to ∼30 Oe for x = 0.04. The relative change, in this case, is ∼46%. It is seen that a slight substitution by the Dy^{3+} dysprosium cations causes a significant decrease in magnetic parameters. The quantities of the spontaneous magnetization and magnetic crystal anisotropy are very required, so they mainly determine the amplitude−frequency characteristics of microwave absorption. The values of these magnetic quantities can be found from the field dependence of magnetization shown in Figure 6 using the so-called approach to saturation.[57,58] The magnetization (M) and magnetic field (H) are correlated by specific ratios. The function of magnetization versus magnetic field $M(H)$ may be written as[59]

$$M = M_s\left(1 - \frac{A}{H} - \frac{A_2}{H^2}\right) - \chi H \quad (4)$$

where M is the magnetization, M_s is the spontaneous magnetization, A is the inhomogeneity parameter, χ is the high field susceptibility, H is the applied field, and A_2 is the anisotropy parameter. The values of A inhomogeneity

https://doi.org/10.1021/acsomega.1c00611
ACS Omega 2021, 6, 10266−10280

parameter and χ susceptibility are negligible $A \to 0$ and $\chi \to 0$ in high magnetic fields $H \to \infty$.[60] The A_2 anisotropy parameter for the cubic structure may be written as[61]

$$A_2 = \frac{8}{105} \times \frac{{k_{eff}}^2}{{M_s}^2} \quad (5)$$

where K_{eff} is the effective magnetic crystal anisotropy coefficient. The 8/105 numerical coefficient holds for random polycrystalline samples with cubic anisotropy.[62] Therefore, the M magnetization may be re-written as[61]

$$M = M_s\left(1 - \frac{8}{105} \times \frac{{k_{eff}}^2}{{M_s}^2} \times \frac{1}{H^2}\right) \quad (6)$$

It can be seen that the A_2 anisotropy parameter is the proportionality coefficient in the $M(H^2)$ linear function, and therefore, it is equal to the tan(α) slope tangent of the linear interpolation of the function $M(H^{-2})$. Therefore, the K_{eff} effective magnetic crystal anisotropy coefficient may be re-written as[61]

$$k_{eff} = \sqrt{\frac{105}{8} \times \tan(\alpha)} \times M_s \quad (7)$$

The H_a anisotropy field and the K_{eff} effective magnetic crystal anisotropy coefficient correlate as follows[61]

$$H_a = 2 \times \frac{k_{eff}}{M_s} \quad (8)$$

The $M(H^{-2})$ dependence was calculated from Figure 1 data to determine the M_s, K_{eff}, and H_a values and are presented in Table 2. The saturation magnetization is the intersection point of the $M(H^{-2})$ function linear extrapolation with the Y-axis. The tangent is found as $\Delta y/\Delta x$ or $\Delta M/\Delta(H^{-2})$. The calculation process is described in our previous article.[63]

Table 2. - Values of M_s Saturation Magnetization, K_{eff}, and H_a for the $[Ni_{0.4}Cu_{0.2}Zn_{0.4}](Fe_{2-x}Dy_x)O_4$ ($0.00 \le x \le 0.04$) SFNPs at T = 300 K

X	M_s, emu/g	tan(α)	K_{eff}, Erg/g	H_a, Oe
0.00	39.85	2.68×10^9	1.87×10^5	9.04×10^3
0.010	45.64	3.07×10^9	2.01×10^5	8.79×10^3
0.02	28.78	4.66×10^9	2.47×10^5	1.27×10^4
0.03	23.78	5.30×10^9	2.64×10^5	2.22×10^4
0.04	18.85	3.55×10^9	2.16×10^5	2.29×10^4

The obtained values of the K_{eff} effective magnetic crystal anisotropy coefficient (see Table 2) are not very large for the cubic crystals, and they are very well correlated with earlier obtained results for the cobalt ferrite nanoparticles as can be seen from Table 3 in ref 61 and Figure 4 in ref 62. The values of the H_a anisotropy field are received by doubling the K_{eff} effective magnetic crystal anisotropy coefficient and dividing by the M_s spontaneous magnetization.

From Figure 6, it can be well seen that the magnetization behavior is not almost linear in strong magnetic fields. This is due to the ongoing para-process. As it can be well seen from Table 2, the maximal value of the M_s saturation magnetization (~46 emu/g) corresponds to SFNPs where x = 0.01. For x = 0.04, the minimal M_s saturation magnetization is observed, which is ~19 emu/g. The values of K_{eff} and H_a were calculated and are also given in Table 2. The results obtained are in good agreement with the previously known ones.[59−62]

Only the M_S spontaneous magnetization changes almost monotonously if the result for the sample with x = 0.01 is not taken into account (Figure 7a).

With an increase in the Dy^{3+} dysprosium cation concentration, the spontaneous magnetization decreases from ~40 emu/g for x = 0.00 down to ~19 emu/g for x = 0.04. The maximum M_S spontaneous magnetization of ~46 emu/g is observed for x = 0.01. The coercive force does not vary monotonously in the range of 56−30 Oe, showing an inflection point at x = 0.02 (Figure 7b). The maximum value of the coercive force of ~73 Oe is observed for x = 0.03. The K_{eff} effective magnetic crystal anisotropy coefficient initially begins to increase from ~ 10^5 Erg/g for x = 0.00 to its maximum value of ~1.41×10^5 Erg/g for x = 0.03, and then it drops down to ~1.16×10^5 Erg/g for x = 0.04. The H_a anisotropy field also has an inflection point of ~9 kOe at x = 0.02. It increases with the increasing substitution concentration from ~5 kOe at x = 0.00 up to ~12 kOe at x = 0.04.[64−66]

It was repeatedly established earlier that the $Fe^{3+}(6)-O^{2-}-Fe^{3+}(6)$ superexchange interactions for the octahedral coordination of iron cations in the orbitally disordered state are positive, whereas for the oxygen deficiency, the cation coordination decreases and the $Fe^{3+}(5)-O^{2-}-Fe^{3+}(5)$ superexchange interactions in the decreased pentahedral coordination become negative.[67,68] In the case of homovalent substitution in the Dy^{3+} cations, the competition in the $Fe^{3+}(6)-O^{2-}-Fe^{3+}(6)$, $Fe^{3+}(5)-O^{2-}-Fe^{3+}(5)$, and $Fe^{3+}(5)-O^{2-}-Dy^{3+}(6)$ superexchange interactions may occur as a result of the destruction of the periodicity of exchange-linked chains. Such competition between antiferromagnetic and ferromagnetic exchange interactions often leads to the distortion of the exchange bonds and a spin glass state with the reduced magnetic parameters.

2.4. Dielectric Properties. To demonstrate the dielectric properties of $[Ni_{0.4}Cu_{0.2}Zn_{0.4}](Fe_{2-x}Dy_x)O_4$ (x = 0.00−0.04) SFNPs, the ε' real part and the ε'' imaginary part of the complex $\varepsilon = \varepsilon' + i\varepsilon''$ permittivity and conductivity at alternating current in the 1 to 3 × 10^6 Hz frequency and 20−120 °C temperature ranges were measured. The spectra of the ε' real part of permittivity for the $[Ni_{0.4}Cu_{0.2}Zn_{0.4}](Fe_{2-x}Dy_x)O_4$ (x = 0.00−0.04) SFNPs are presented in Figure 8a−e.

As it is already known, the dielectric properties of ferrites are determined by their own stoichiometry, impurities, crystal structure, ceramic morphology, external signal frequency, temperature, and even humidity.[69]

To avoid the influence of moisture, the sample was preheated to 120 °C and held for 10 min, followed by cooling to the required measurement temperature at the beginning of the measurement cycle. It is obvious that the spectra of the ε' real part of permittivity decrease with the increase of frequency for all the concentrations at all temperatures, demonstrating a normal ferrimagnetic behavior.[70] At high frequencies, the values of the ε' real part of permittivity practically coincide for all temperatures as it has been reported previously.[71] At low frequencies, the values are different and non-monotonically depend on temperature. This behavior is associated with the accumulation of charge carriers at the electrode−sample interface.[72] The polarization of the electrode and grain boundaries at low frequencies is determined as the Maxwell−Wagner polarization.[73]

https://doi.org/10.1021/acsomega.1c00611
ACS Omega 2021, 6, 10266−10280

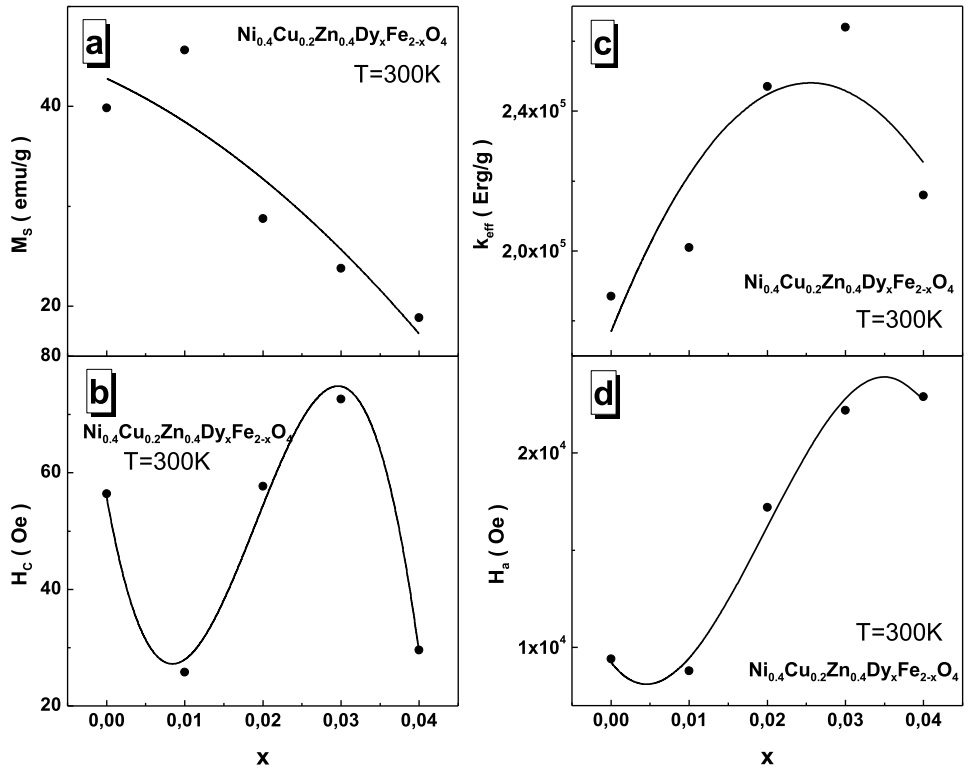

Figure 7. Spontaneous magnetization—M_s (a), coercive force—H_C (b), K_{eff} (c), and H_a (d) depending on the dysprosium ion concentration in the $[Ni_{0.4}Cu_{0.2}Zn_{0.4}](Fe_{2-x}Dy_x)O_4$ ($0.00 \leq x \leq 0.04$) SFNPs at T = 300 K.

The behavior of the spectra with increasing temperature depends on the substitution concentration by Dy^{3+} dysprosium cations. Thus, for the x = 0.00, 0.01, 0.02, and 0.03 samples, the value increases, while for x = 0.04, the value decreases with the increasing temperature. The temperature dependencies of the ε' real part of permittivity at a low frequency have a minimum point for x = 0.00, 0.01, and 0.03, a maximum point for x = 0.02, and an inflection point for x = 0.04 (see insets of Figure 7) where the extreme points are observed in the range of 60−90 °. The maximum value of the ε' real part of permittivity varies from ∼1.8 for x = 0.00 up to ∼81 for x = 0.03 at 1 Hz. In general, with increasing substitution concentration, the consistent increases to the maximum value at low frequencies.

The spectra of the ε'' imaginary part of permittivity for the studied $[Ni_{0.4}Cu_{0.2}Zn_{0.4}](Fe_{2-x}Dy_x)O_4$ (x = 0.00−0.04) SFNPs are shown in Figure 9. The values of the ε'' imaginary part of permittivity at high frequencies are almost the same and minimal except for the initial unsubstituted sample (x = 0.00). An abnormal increase in the imaginary part is observed for this sample at high temperatures. The maximum values of the ε''/ imaginary part of permittivity are also observed at low frequencies, and they vary from ∼0.3 for x = 0.00 up to ∼161 for x = 0.03. With the increasing temperature, the change in magnitude is also non-monotonic.

The value increases for x = 0.00, 0.02, and 0.03 and decreases for 0.04. It should be noted that for x = 0.00, a peak appears in the spectrum at temperatures of 100−120 °C.·In the temperature dependencies at a low frequency, a minimum point is detected for x = 0.03 and an inflection point is detected for x = 0.00 and 0.04 (see the insets of Figure 9). For x = 0.02, a monotonic increase in the ε'' imaginary part of permittivity at 1 Hz is observed. In general, there is a steady growth of the low-frequency value of the ε'' imaginary part of permittivity with the increased value of x.

Despite the large values of the ε'' imaginary part of permittivity, the tan(δ) dielectric loss tangent is not very large, and it varies from ∼0.2 for x = 0.00 to ∼2.6 for x = 0.04. Noteworthy is the noticeable increase in the tan(δ) dielectric loss tangent for x = 0.00 above 10^5 Hz, while for all other samples, its change is almost imperceptible at high frequencies. In addition, a peak at low frequencies appears for this sample at temperatures of 90−120 °C. The maximum tan(δ) dielectric loss tangent values are observed at low frequencies. The temperature behavior of the low-frequency component is increasing for x = 0.00, 0.02, and 0.03 and decreasing for x = 0.04. In the temperature dependences at 1 Hz, a minimum point is observed for x = 0.03 and 0.04 (see the insets in Figure 10).

An inflection point is found for x = 0.00 and 0.04. The temperature dependency is characterized by a monotonic increase for x = 0.02. In general, the maximum value of the tan(δ) dielectric loss tangent steadily increases with the increasing substitution concentration. From the analysis of changes in the amplitude−frequency characteristics of the samples studied, it can be concluded that the substitution by Dy^{3+} dysprosium cations even in small amounts leads to noticeable changes in dielectric properties. This is due to the ionic size and electronic configuration of the indicated Dy^{3+} dysprosium cation. The ionic radius of the Dy^{3+} dysprosium cation in the octahedral coordination is ∼0.91 Å, which is almost twice the ionic radius of Fe^{3+} (∼0.64 Å) in the same coordination site.

The size effect causes severe distortion of the crystal lattice, which complicates the electronic hopping in the Dy^{3+}−O^{2-}−Fe^{3+} dysprosium−oxygen−iron exchange chains. In addition,

https://doi.org/10.1021/acsomega.1c00611
ACS Omega 2021, 6, 10266−10280

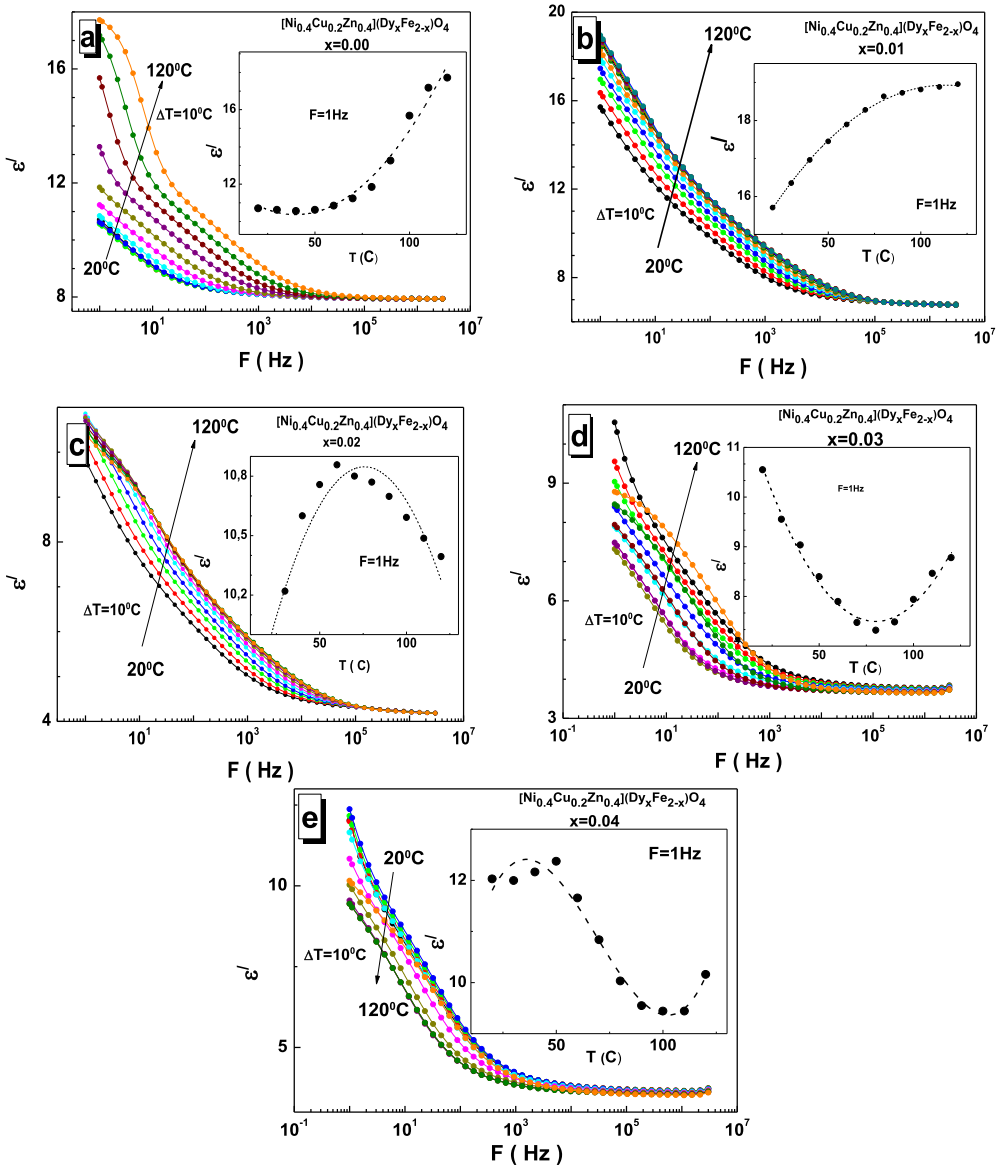

Figure 8. Frequency dependences of the ε' real part of permittivity in the range of 1 to 3 × 10^6 Hz at different temperatures from 20 °C up to 120 C with a step of ΔT = 10 °C for $[Ni_{0.4}Cu_{0.2}Zn_{0.4}](Fe_{2-x}Dy_x)O_4$ ($0.00 \leq x \leq 0.04$) SFNPs. (a) x = 0.00, (b) x = 0.01, (c) x = 0.02, (d) x = 0.03, and (e) x = 0.04. The insets demonstrate the temperature dependency of ε' at F = 1 Hz.

the external electrons of the Dy^{3+} dysprosium cation are more localized than the external electrons of the Fe^{3+} iron cation, which improves the dielectric constant and reduces the conductivity.

2.5. Microwave Properties. The described approach explains the results of the microwave property investigations for $[Ni_{0.4}Cu_{0.2}Zn_{0.4}](Fe_{2-x}Dy_x)O_4$ (x = 0.00−0.04) SFNPs. The *S*-parameters were examined as described in ref 7. From *S*-parameters, the permittivity and permeability values have been determined using the Nicholson−Ross−Weir (NRW) algorithm.[74] According to the calculated values of the real and imaginary parts of the dielectric permittivity and magnetic permeability, the reflection coefficient was calculated using the formula for calculating the reflection coefficient from the material layer. The obtained permittivity and permeability frequency dispersions made it possible to notice the intensive electromagnetic absorption in the 1−3 GHz frequency range. Figure 10 displays the frequency dependencies of the reflection losses in the mentioned frequency range. The calculated values of reflection losses indicate absorption processes in the range of 1.6−2.7 GHz (Figure 11).

There are some mechanisms for a resonant electromagnetic absorption in complex magnetic oxides. One of them is the domain boundaries resonance. The second mechanism is concerned with natural ferromagnetic resonance (NFR). The resonance of the domain boundary may underlie electromagnetic absorption. Any domain wall (e.g., string or a rigid membrane) is usually characterized by its own frequency of the oscillation. The forcing electromagnetic resonance (EMR) will acquire a frequency close to that of a domain wall with an increase in its frequency. This phenomenon can lead to resonance, which in turn leads to intense electromagnetic energy absorption. The length and elasticity of the domain wall are factors that determine its frequency. The domain boundary elasticity is usually higher for smaller domains with short boundary length. Thus, the frequency of resonant EMR absorption is higher due to short and elastic boundary. As a result, we can conclude that the control of the resonant

https://doi.org/10.1021/acsomega.1c00611
ACS Omega 2021, 6, 10266−10280

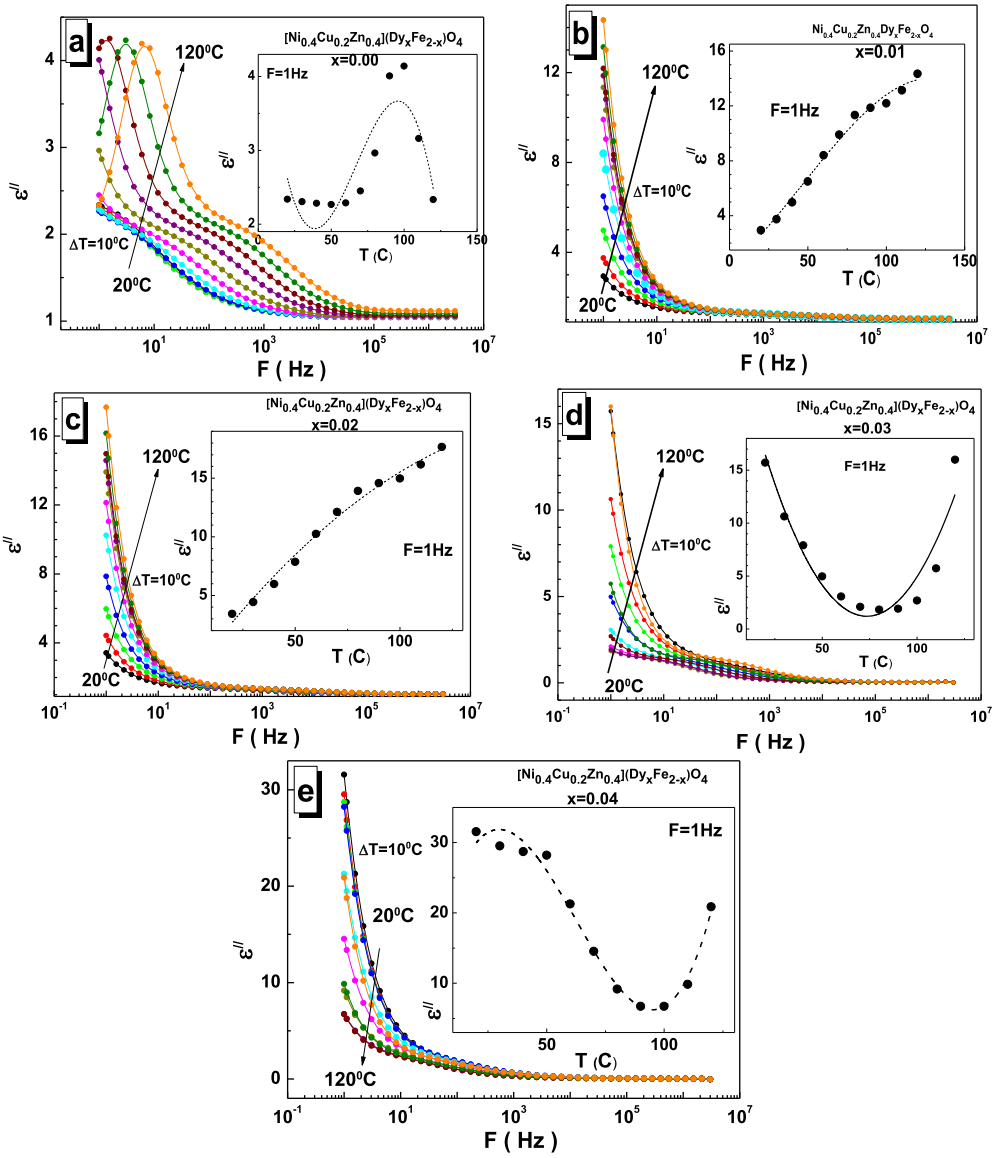

Figure 9. Frequency dependences of the ε'' imaginary part of permittivity in the range of 1 to 3 × 10^6 Hz at different temperatures from 20 °C up to 120 °C with a step of ΔT = 10 °C $[Ni_{0.4}Cu_{0.2}Zn_{0.4}](Fe_{2-x}Dy_x)O_4$ ($0.00 \leq x \leq 0.04$) SFNPs. (a) x = 0.00, (b) x = 0.01, (c) x = 0.02, (d) x = 0.03, and (e) x = 0.04. Insets demonstrate the temperature dependency of the ε'' at F = 1 Hz.

frequency can be performed by varying the domain size. The two simplest and most widely known methods of this change are as follows:

(1) the magnetic structure distortion caused by the long-range order of exchange interactions change and

(2) variation in crystallite size.

The substitution of the magnetic ion by the larger ion may cause the above changes. In the case of Dy^{3+}-substituted Ni−Cu−Zn spinels, we observed a good correlation between the chemical composition (amount of the Dy^{3+} ions), APS, and microwave properties.

The main amplitude−frequency characteristics $[Ni_{0.4}Cu_{0.2}Zn_{0.4}](Fe_{2-x}Dy_x)O_4$ (x = 0.00−0.04) SFNPs are presented in Figure 12.

The minimum (peak) on frequency dependencies of the R_L (reflection losses) can be explained as the resonant amplitude (A_{Res}) that corresponds to the maximal value of the absorbed electromagnetic energy. The position of A_{Res} in the frequency range is the resonant frequency (F_{Res}). It corresponds to the frequency of the maximal electromagnetic absorption. The width of resonance—W_{Res}—is equal to the width value at the 1/2 value of A_{Res}. For the unsubstituted sample (x = 0.00), the maximal electromagnetic absorption (−40.6 dB) was observed at 2.57 GHz. A rise of the Dy^{3+} concentration from x = 0.01 to 0.05 leads to a decrease in the resonant frequency from 2.12 to 1.65 GHz. For all investigated samples, the maximum value of A_{Res} was detected for the x = 0.01 composition as −57.3 dB. Furthermore, the average A_{Res} changed non-linearly when Dy^{3+} was added to the composition (transition from x = 0.00 to x = 0.01). This finding is well associated with the microstructure analysis and the explanation provided earlier. From our point of view, the value of F_{Res} is determined by the features of microstructure and because of the domain size and peculiarities of the domain wall. At the same time, the value of A_{Res} is determined by the features of the magnetic structure (intensity of the exchange interaction due to Dy^{3+} ion distribution and distortion of the magnetic structure). Thus,

https://doi.org/10.1021/acsomega.1c00611
ACS Omega 2021, 6, 10266−10280

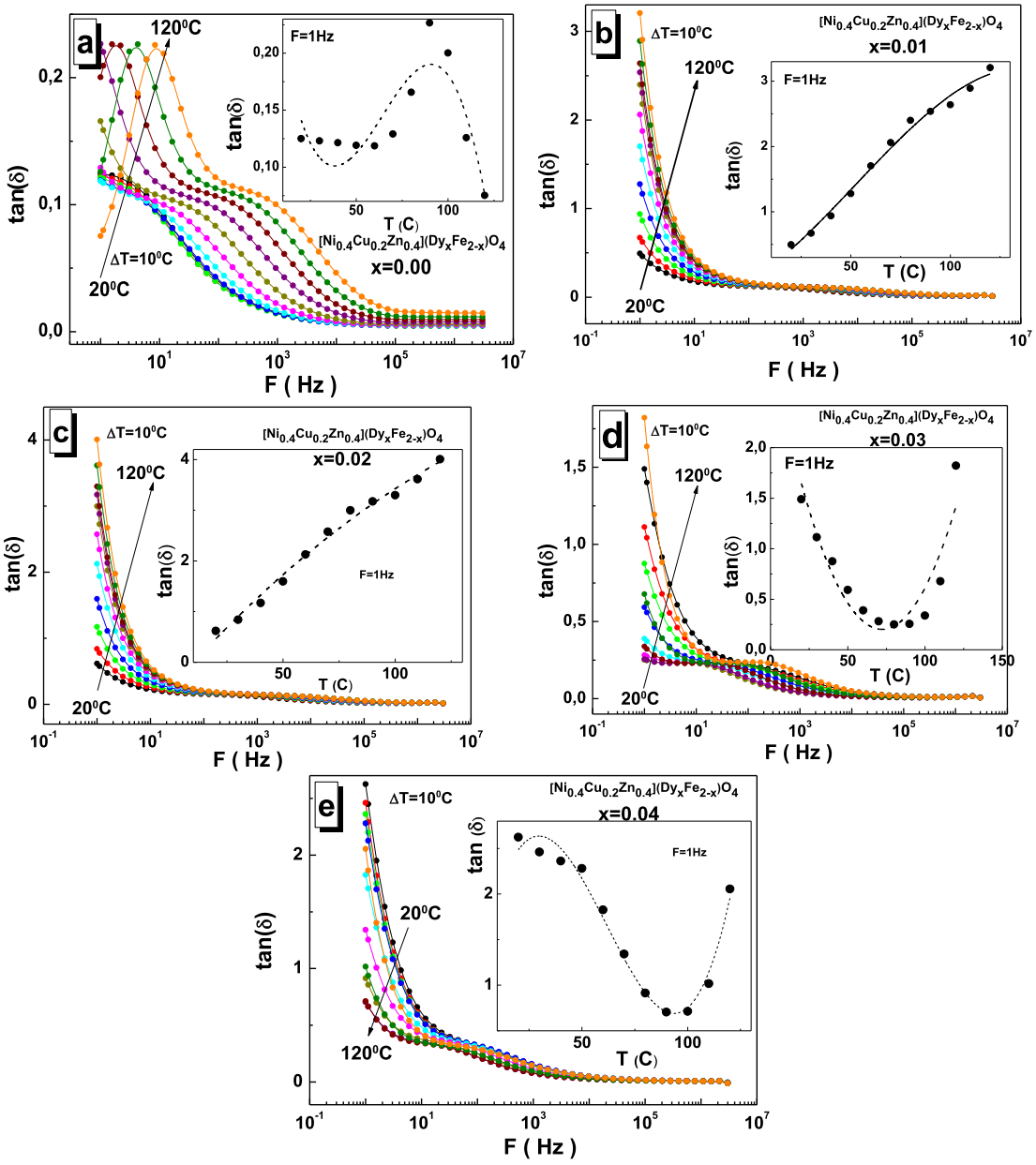

Figure 10. Frequency dependences of tan(δ) dielectric loss tangent in the range of 1 Hz to 3 × 10^6 Hz at different temperatures from 20 °C up to 120 °C with a step of ΔT = 10 °C for $[Ni_{0.4}Cu_{0.2}Zn_{0.4}](Fe_{2-x}Dy_x)O_4$ ($0.00 \leq x \leq 0.04$) SFNPs. (a) x = 0.00, (b) x = 0.01, (c) x = 0.02, (d) x = 0.03, and (e) x = 0.04. The insets demonstrate the temperature dependency of tan(δ) at F = 1 Hz.

significant changes in the amplitude between x = 0.00 and x = 0.01 were observed. The value of W_{Res} or the width of the peak depends on the APS dispersion. Usually, a significant dispersion of grain and crystallite sizes is observed in the samples. The corresponding dispersion is typical for the size of the domain boundaries. As a result, each domain will have its own unique frequency.

Therefore, the magnetic loss area in terms of electromagnetic energy depends on the peaks of the individual domain wall. It can be concluded that the wider the dispersion of crystallite sizes, the larger the reflection coefficient area for a given material will be due to the blurring of the resonance frequency of domain walls. In the case of Dy^{3+} substitution, we observed narrow absorption peaks, which correlate well with the APS dispersion. For all samples, a low APS dispersion results in close values of the W_{Res}.

3. CONCLUSIONS

Spinel ferrite nanoparticles with nominal compositions ($[Ni_{0.4}Cu_{0.2}Zn_{0.4}](Fe_{2-x}Dy_x)O_4$ (x = 0.00−0.04) SFNPs) were synthesized by a citrate sol−gel auto-combustion method. It was established that the increase of the Dy^{3+} concentration leads to an increase of the lattice parameters, which can be explained by the differences of the ionic radii of the Fe^{3+} and Dy^{3+} ions. The microstructural analysis shows that the maximum particle size value is observed at x = 0.03 (19 nm) and the minimum at x = 0.00 (15 nm). The ^{57}Fe Mössbauer results revealed that the Dy^{3+} (0.91 Å) ion prefers to occupy the octahedral B site due to its large ionic radius. The nonlinear behavior of the main magnetic parameters in $[Ni_{0.4}Cu_{0.2}Zn_{0.4}](Fe_{2-x}Dy_x)O_4$ ($0.00 \leq x \leq 0.04$) SFNPs was observed. It can be concluded that the substitution by Dy^{3+} dysprosium cations even in small amounts leads to noticeable

https://doi.org/10.1021/acsomega.1c00611
ACS Omega 2021, 6, 10266−10280

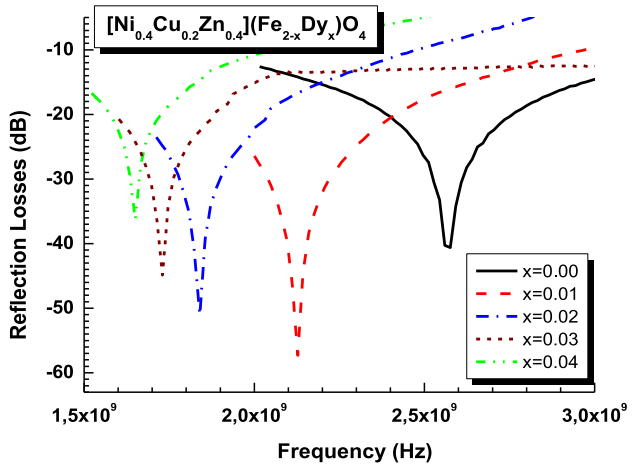

Figure 11. Frequency dependences of the reflection losses of the $[Ni_{0.4}Cu_{0.2}Zn_{0.4}](Fe_{2-x}Dy_x)O_4$ ($0.00 \le x \le 0.04$) SFNPs.

changes in dielectric properties. The explanation of the correlation of the magnetic/electrical properties was given in terms of the features of $Dy^{3+}-O^{2-}-Fe^{3+}$ dysprosium–oxygen–iron indirect exchange. This is due to the ionic size and electronic configuration of the indicated Dy^{3+} dysprosium cation. Microwave properties have been determined in wide frequencies from 1 GHz to 20 GHz. The occurrences of the intensive electromagnetic absorption in the frequencies from 1.6 to 2.7 GHz were observed. The maximum electromagnetic absorption (−40.6 dB) was observed for the unsubstituted sample (x = 0.00) at 2.57 GHz. An increase of the Dy^{3+} concentration from x = 0.01 to 0.04 leads to a decrease in the resonant frequency from 2.12 to 1.65 GHz. For all the investigated samples, the maximum value A_{Res} was detected as −57.3 dB for x = 0.01. In the case of Dy^{3+} substitution, we observed narrow absorption peaks that correlate well with the APS dispersion.

4. EXPERIMENTAL SECTION

$[Ni_{0.4}Cu_{0.2}Zn_{0.4}](Fe_{2-x}Dy_x)O_4$ ($0.00 \le x \le 0.04$) SFNPs with different Dy^{3+} amounts were prepared by the citrate sol–gel auto-combustion technique.[75,76] The chlorides and nitrates of Ni^{2+}, Zn^{2+}, Cu^{2+}, Fe^{3+}, and Dy^{3+} $NiCl_2{\cdot}6H_2O$, $Zn(NO_3)_2$, $Cu(NO_3)_2$, $Fe(NO_3)_3{\cdot}9H_2O$, $Dy(NO_3)_3$, and citric acid ($C_6H_8O_7$) were used for nanosized $[Ni_{0.4}Cu_{0.2}Zn_{0.4}]$-$(Fe_{2-x}Dy_x)O_4$ ($0.00 \le x \le 0.04$) SFNPs production. The ratios of the initial components were calculated based on the following equation

$$0.4Ni^{2+} + 0.4Zn^{2+} + 0.2Cu^{2+} + xDy^{3+} + (2 - x)Fe^{3+} \rightarrow [Ni_{0.4}Cu_{0.2}Zn_{0.4}](Fe_{2-x}Dy_x)O_4 \quad (9)$$

The number of moles metal salts used during the synthesis is provided in Table 3. The ratios of the initial components were calculated based on the following equation:

All salts in stoichiometric ratios were dissolved in 50 mL of deionized water, followed by stirring at 85 °C for 45 min. The pH of both solutions was regulated at 7 with ammonia and tuning the temperature to 180 °C, which was kept for 50 min, and then the system was heated up to 370 °C to yield a black powder. The final powders were calcined at 950 °C for 2 h. Crystal structure parameters were obtained by an X-ray diffractometer in Cu Kα radiation using a Rigaku Benchtop

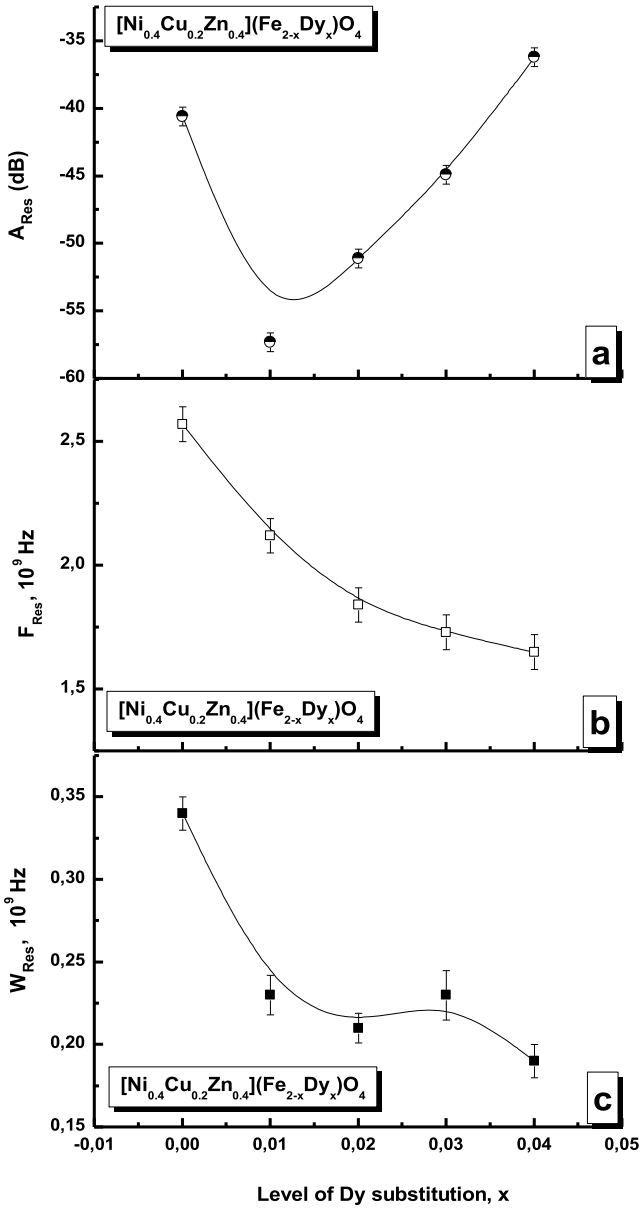

Figure 12. Frequency dependences of the main amplitude–frequency characteristics of the $[Ni_{0.4}Cu_{0.2}Zn_{0.4}](Fe_{2-x}Dy_x)O_4$ ($0.00 \le x \le 0.04$) SFNPs: (a) resonant amplitude(A_{Res}); (b) resonant frequency (F_{Res}); and (c) width of the resonance (W_{Res}).

Table 3. Number Moles of Metal Salts for the Synthesis of $[Ni_{0.4}Cu_{0.2}Zn_{0.4}](Fe_{2-x}Dy_x)O_4$ ($0.00 \le x \le 0.04$) SFNPs[a]

X	0.00	0.01	0.02	0.03	0.04
Ni (mole)	0.4	0.4	0.4	0.4	0.4
Zn (mole)	0.4	0.4	0.4	0.4	0.4
Cu (mole)	0.2	0.2	0.2	0.2	0.2
Fe (mole)	2	1.99	1.98	1.97	1.96
Dy (mole)		0.01	0.02	0.03	0.04

[a](3 mol of citric acid was used for all x ratios).

Miniflex XRD analyzer, Japan (Cu Kα radiation at room temperature, λ = 1.5406 Å, 2θ = 20–70°, step 0.02 (deg) with scanning rate 5.0 (deg/min)). The unit cell parameters were calculated from XRD data using Rietveld refinements. The relevance factors of Rietveld refinements were in the range R_{wp}

https://doi.org/10.1021/acsomega.1c00611
ACS Omega 2021, 6, 10266–10280

= 10.7−14.1; R_{exp} = 7.37−10.2; and χ^2 = 1.12−2.14. The microstructure analysis was performed using the SEM images obtained from a Zeiss EVO 10 (Zeiss, Germany). The Mössbauer spectra were obtained at room temperature via a spectrometer operated in the constant acceleration mode using the radiation source 50mCi 57Co (Rh matrix) in the transmission geometry (UNIVEM MS software). The magnetic properties were analyzed via vibrating sample magnetometry at 300 K with applying field H = ±70 kOe. The electrical properties were investigated via a Novocontrol Alpha-N high-resolution impedance analyzer (Germany) between the temperatures from 20 to 120 °C and a frequency ranging from 1 Hz to 3 MHz. To measure the electrical properties, the samples were made in the form of a parallelepiped with dimensions of 2 × 2 × 10 mm. Because of the high resistivity, measurements were taken using the standard two-probe method. The frequency dependency of S-parameters was achieved by an Agilent network analyzer with frequencies ranging between 1 and 4.5 GHz and calculated by an NRW manner.[68] The MW reflection loss has been calculated via[76]

$$\dot{R} = \frac{\sqrt{\frac{\dot{\mu}}{\dot{\varepsilon}}} - 1}{\sqrt{\frac{\dot{\mu}}{\dot{\varepsilon}}} + 1} \text{ or } |\dot{R}| = 20 \lg\left(\frac{\sqrt{\frac{\dot{\mu}}{\dot{\varepsilon}}} - 1}{\sqrt{\frac{\dot{\mu}}{\dot{\varepsilon}}} + 1}\right) \text{ in dB} \quad (10)$$

where $|\dot{R}|$ (in dB) is the reflection coefficient modulus defined as the reflected ratio to incident wave amplitude.[50]

AUTHOR INFORMATION

Corresponding Author

Alex Trukhanov − *Laboratory of Magnetic Films Physics, Scientific-Practical Materials Research Centre of National Academy of Sciences of Belarus, Minsk 220072, Belarus; Laboratory of Single Crystal Growth, South Ural State University, Chelyabinsk 454080, Russia;* orcid.org/0000-0003-3430-9578; Email: truhanov86@mail.ru

Authors

Munirah Abdullah Almessiere − *Department of Biophysics, Institute for Research and Medical Consultations (IRMC), Imam Abdulrahman Bin Faisal University, Dammam 31441, Saudi Arabia*

Yassine Slimani − *Department of Biophysics, Institute for Research and Medical Consultations (IRMC), Imam Abdulrahman Bin Faisal University, Dammam 31441, Saudi Arabia;* orcid.org/0000-0002-2579-1617

Hakan Güngüneş − *Department of Physics, Hitit University, Bulvarı-Çorum 19030, Turkey*

Ayse Demir Korkmaz − *Department of Chemistry, Istanbul Medeniyet University, Uskudar-Istanbul 34700, Turkey*

Tatiana Zubar − *Laboratory of Magnetic Films Physics, Scientific-Practical Materials Research Centre of National Academy of Sciences of Belarus, Minsk 220072, Belarus; Laboratory of Single Crystal Growth, South Ural State University, Chelyabinsk 454080, Russia;* orcid.org/0000-0002-2225-9641

Sergei Trukhanov − *Laboratory of Magnetic Films Physics, Scientific-Practical Materials Research Centre of National Academy of Sciences of Belarus, Minsk 220072, Belarus*

Ayyar Manikandan − *Department of Chemistry, Bharath Institute of Higher Education and Research (BIHER), Bharath University, Chennai 600073, India*

Fatimah Alahmari − *Department of Nanomedicine, Institute for Research and Medical Consultations (IRMC), Imam Abdulrahman Bin Faisal University, Dammam 31441, Saudi Arabia*

Abdulhadi Baykal − *Department of Nanomedicine, Institute for Research and Medical Consultations (IRMC), Imam Abdulrahman Bin Faisal University, Dammam 31441, Saudi Arabia*

Complete contact information is available at: https://pubs.acs.org/10.1021/acsomega.1c00611

Notes

The authors declare no competing financial interest.

ACKNOWLEDGMENTS

The authors are thankful to the Institute for Research and Medical Consultations (IMRC) of Imam Abdulrahman Bin Faisal University (IAU—Saudi Arabia) for providing lab facilities. This work was financially supported by the Deanship for Scientific Research (Project application no. 2020-164-IRMC) of Imam Abdulrahman Bin Faisal University (IAU—Saudi Arabia).

REFERENCES

(1) Jung, Y. H.; Lee, J.; Qiu, Y.; Cho, N.; Cho, S. J.; Zhang, H.; Lee, S.; Kim, T. J.; Gong, S.; Ma, Z. Stretchable Twisted-Pair Transmission Lines for Microwave Frequency Wearable Electronics. *Adv. Funct. Mater.* **2016**, *26*, 4635−4642.

(2) Celozzi, S.; Araneo, R.; Lovat, G. *Electromagnetic Shielding. Wiley Series in Microwave and Optical Engineering*; Wiley: New Jersey, 2008 pp 21−38.

(3) Almessiere, M. A.; Slimani, Y.; Baykal, A. Structural, morphological and magnetic properties of hard/soft $SrFe_{12-x}V_xO_{19}/(Ni_{0.5}Mn_{0.5}Fe_2O_4)_y$ nanocomposites: Effect of vanadium substitution. *J. Alloys Compd.* **2018**, *767*, 966−975.

(4) Dippong, T.; Levei, E. A.; Cadar, O.; Goga, F.; Toloman, D.; Borodi, G. Thermal behavior of Ni, Co and Fe succinates embedded in silica matrix. *J. Therm. Anal. Calorim.* **2019**, *136*, 1587−1596.

(5) Dippong, T.; Levei, E. A.; Cadar, O.; Goga, F.; Borodi, G.; Barbu-Tudoran, L.; Lucian, B. Thermal behavior of CoxFe3−xO4/SiO2 nanocomposites obtained by a modified sol-gel method. *J. Therm. Anal. Calorim.* **2017**, *128*, 39−52.

(6) Ketsko, V. A.; Beresnev, E. N.; Kop'eva, M. A.; Elesina, L. V.; Baranchikov, A. I.; Stognii, A. I.; Trukhanov, A. V.; Kuznetsov, N. T. Specifics of pyrohydrolytic and solid-phase syntheses of solid solutions in the (MgGa2O4) x (MgFe2O4)1 − x system. *Russ. J. Inorg. Chem.* **2010**, *55*, 427−429.

(7) Almessiere, M. A.; Trukhanov, A. V.; Slimani, Y.; You, K. Y.; Trukhanov, S. V.; Trukhanova, E. L.; Esa, F.; Sadaqat, A.; Chaudhary, K.; Zdorovets, M.; Baykal, A. Correlation between composition and electrodynamics properties in nanocomposites based on hard/soft ferrimagnetics with strong exchange coupling. *Nanomaterials* **2019**, *9*, 202.

(8) Darwish, M. A.; Trukhanov, A. V.; Senatov, O. S.; Morchenko, A. T.; Saafan, S. A.; Astapovich, K. A.; Trukhanov, S. V.; Trukhanova, E. L.; Pilyushkin, A. A.; Sombra, A. S. B.; Zhou, D.; Jotania, R. B.; Singh, C. Investigation of AC-measurements of epoxy/ferrite composites. *Nanomaterials* **2020**, *10*, 492−516.

(9) Benrabaa, R.; Boukhlouf, H.; Löfberg, A.; Rubbens, A.; Vannier, R.-N.; Bordes-Richard, E.; Barama, A. Nickel ferrite spinel as catalyst precursor in the dry reforming of methane: synthesis, characterization and catalytic properties. *J. Nat. Gas Chem.* **2012**, *21*, 595−604.

(10) Houlding, T. K.; Rebrov, E. V. Application of alternative energy forms in catalytic reactor engineering. *Green Process. Synth.* **2012**, *1*, 19−31.

(11) Rebrov, E. V.; Gao, P.; Verhoeven, T. M. W. G. M.; Schouten, J. C.; Kleismit, R.; Turgut, Z.; Kozlowski, G. Structural and magnetic properties of sol-gel Co2xNi0.5−x Zn0.5−xFe2O4 thin films. *J. Magn. Magn. Mater.* **2011**, *323*, 723−729.
(12) Gao, P.; Rebrov, E. V.; Verhoeven, T. M. W. G. M.; Schouten, J. C.; Kleismit, R.; Kozlowski, G.; Cetnar, J.; Turgut, Z.; Subramanyam, G. Structural investigations and magnetic properties of sol-gel Ni0.5Zn0.5Fe2O4 thin films for microwave heating. *J. Appl. Phys.* **2010**, *107*, 044317.
(13) Gao, P.; Hua, X.; Degirmenci, V.; Rooney, D.; Khraisheh, M.; Pollard, R.; Bowman, R. M.; Rebrov, E. V. Structural and magnetic properties of Ni1−xZnxFe2O4 (x=0, 0.5 and 1) nanopowders prepared by sol-gel method. *J. Magn. Magn. Mater.* **2013**, *348*, 44−50.
(14) Kozlovskiy, A. L.; Zdorovets, M. V. The study of the structural characteristics and catalytic activity of Co/CoCo2O4 nanowires. *Composites, Part B* **2020**, *191*, 107968.
(15) Kozlovskiy, A. L.; Kenzhina, I. E.; Zdorovets, M. V. FeCo-Fe2CoO4/Co3O4 nanocomposites: Phase transformations as a result of thermal annealing and practical application in catalysis. *Ceram. Int.* **2020**, *46*, 10262−10269.
(16) Zdorovets, M. V.; Kozlovskiy, A. L. Study of phase transformations in Co/CoCo2O4 nanowires. *J. Alloys Compd.* **2020**, *815*, 152450.
(17) Zdorovets, M. V.; Kozlovskiy, A. L. Investigation of phase transformations and corrosion resistance in Co/$CoCo_2O_4$ nanowires and their potential use as a basis for lithium-ion batteries. *Sci. Rep.* **2019**, *9*, 16646.
(18) Kozlovskiy, A.; Zdorovets, M. Study of the applicability of directional modification of nanostructures to improve the efficiency of their performance as the anode material of lithium-ion batteries. *Mater. Res. Express* **2019**, *6*, 075066.
(19) Kumar, M.; Singh Dosanjh, H.; Sonika; Singh, J.; Monir, K.; Singh, H. Review on magnetic nanoferrites and their composites as alternatives in waste water treatment: synthesis, modifications and applications. *Environ. Sci.: Water Res. Technol.* **2020**, *6*, 491−514.
(20) Xianfeng, C.; Dongli, J.; Chenmou, Z. The preparation and gas-sensing properties of $NiFe_2O_4$ nanocubes and nanorods. *Sens. Actuators, B* **2007**, *123*, 793−797.
(21) Darshane, S. L.; Suryavanshi, S. S.; Mulla, I. S. Nanostructured nickel ferrite: a liquid petroleum gas sensor. *Ceram. Int.* **2009**, *35*, 1793−1797.
(22) Rashad, M. M.; Fouad, O. A. Synthesis and characterization of nano-sized nickel ferrites from fly ash for catalytic oxidation of CO. *Mater. Chem. Phys.* **2005**, *94*, 365−370.
(23) Rana, S.; Srivastava, R. S.; Sorensson, M. M.; Misra, R. D. K. Synthesis and characterization of nanoparticles with magnetic core and photocatalytic shell: Anatase TiO2-NiFe2O4 system. *Mater. Sci. Eng., B* **2005**, *119*, 144−151.
(24) Kulkarni, A. M.; Desai, U. V.; Pandit, K. S.; Kulkarni, M. A.; Wadgaonkar, P. P. Nickel ferrite nanoparticles-hydrogen peroxide: a green catalyst-oxidant combination in chemoselective oxidation of thiols to disulfides and sulfides to sulfoxides. *RSC Adv.* **2014**, *4*, 36702−36707.
(25) Sunny, V.; Kurian, P.; Mohanan, P.; Joy, P. A.; Anantharaman, M. R. A flexible microwave absorber based on nickel ferrite nanocomposite. *J. Alloys Compd.* **2010**, *489*, 297−303.
(26) McDonald, K. J.; Choi, K.-S. Synthesis and Photoelectrochemical Properties of Fe2O3/ZnFe2O4Composite Photoanodes for Use in Solar Water Oxidation. *Chem. Mater.* **2011**, *23*, 4863−4869.
(27) Lu, G.; Li, S. Hydrogen production by H2S photodecomposition on ZnFe2O4 catalyst. *Int. J. Hydrogen Energy* **1992**, *17*, 767−770.
(28) Lv, H.; Ma, L.; Zeng, P.; Ke, D.; Peng, T. Synthesis of floriated ZnFe2O4 with porous nanorod structures and its photocatalytic hydrogen production under visible light. *J. Mater. Chem.* **2010**, *20*, 3665.
(29) Bid, S.; Pradhan, S. K. Characterization of crystalline structure of ball-milled nano-Ni-Zn-ferrite by Rietveld method. *Mater. Chem. Phys.* **2004**, *84*, 291−301.
(30) Deka, S.; Joy, P. A. Characterization of nanosized NiZn ferrite powders synthesized by an autocombustion method. *Mater. Chem. Phys.* **2006**, *100*, 98−101.
(31) Akhtar, S.; Rehman, S.; Almessiere, M. A.; Khan, F. A.; Slimani, Y.; Baykal, A. Synthesis of Mn0.5Zn0.5SmxEuxFe1.8−2xO4 Nanoparticles via the Hydrothermal Approach Induced Anti-Cancer and Anti-Bacterial Activities. *Nanomater* **2019**, *9*, 1635.
(32) Mathur, P.; Thakur, A.; Lee, J. H.; Singh, M. Sustained electromagnetic properties of Ni-Zn-Co nanoferrites for the high-frequency applications. *Mater. Lett.* **2010**, *64*, 2738−2741.
(33) Chakrabarti, P. K.; Nath, B. K.; Brahma, S.; Das, S.; Goswami, K.; Kumar, U.; Mukhopadhyay, P. K.; Das, D.; Ammar, M.; Mazaleyrat, F. Magnetic and hyperfine properties of nanocrystalline Ni0.2Zn0.6Cu0.2Fe2O4prepared by a chemical route. *J. Phys.: Condens. Matter* **2006**, *18*, 5253.
(34) Batoo, K. M.; Ansari, M. S. Low temperature-fired Ni-Cu-Zn ferrite nanoparticles through auto-combustion method for multilayer chip inductor applications. *Nanoscale Res. Lett.* **2012**, *7*, 112.
(35) Reddy, M. P.; Madhuri, W.; Reddy, N. R.; Kumar, K. V. S.; Murthy, V. R. K.; Reddy, R. R. Influence of copper substitution on magnetic and electrical properties of MgCuZn ferrite prepared by microwave sintering method. *Mater. Sci. Eng., C* **2010**, *30*, 1094−1099.
(36) Ghasemi, A. Particle size dependence of magnetic features for Ni 0.6−x Cu x Zn 0.4 Fe 2 O 4 spinel nanoparticles. *J. Magn. Magn. Mater.* **2014**, *360*, 41−47.
(37) Jacobo, S. E.; Bercoff, P. G. Structural and electromagnetic properties of yttrium-substituted Ni-Zn ferrites. *Ceram. Int.* **2016**, *42*, 7664−7668.
(38) Liu, Z.; Peng, Z.; Lv, C.; Fu, X. Doping effect of Sm 3+ on magnetic and dielectric properties of Ni-Zn ferrites. *Ceram. Int.* **2017**, *43*, 1449−1454.
(39) Qian, K.; Yao, Z.; Lin, H.; Zhou, J.; Haidry, A. A.; Qi, T.; Chen, W.; Guo, X. The influence of Nd substitution in Ni-Zn ferrites for the improved microwave absorption properties. *Ceram. Int.* **2020**, *46*, 227−235.
(40) Eltabey, M. M.; El-Shokrofy, K. M.; Gharbia, S. A. Enhancement of the magnetic properties of Ni-Cu-Zn ferrites by the non-magnetic Al3+-ions substitution. *J. Alloys Compd.* **2011**, *509*, 2473−2477.
(41) Harzali, H.; Saida, F.; Marzouki, A.; Megriche, A.; Baillon, F.; Espitalier, F.; Mgaidi, A. Structural and magnetic properties of nano-sized NiCuZn ferrites synthesized by co-precipitation method with ultrasound irradiation. *J. Magn. Magn. Mater.* **2016**, *419*, 50−56.
(42) Tholkappiyan, R.; Vishista, K. Influence of lanthanum on the optomagnetic properties of zinc ferrite prepared by combustion method. *Phys. B* **2014**, *448*, 177−183.
(43) Trukhanov, A. V.; Algarou, N. A.; Slimani, Y.; Almessiere, M. A.; Baykal, A.; Tishkevich, D. I.; Vinnik, D. A.; Vakhitov, M. G.; Klygach, D. S.; Silibin, M. V.; Zubar, T. I.; Trukhanov, S. V. Peculiarities of the microwave properties of hard-soft functional composites SrTb0.01Tm0.01Fe11.98O19-AFe2O4 (A = Co, Ni, Zn, Cu, or Mn). *RSC Adv.* **2020**, *10*, 32638−32651.
(44) Kabbur, S. M.; Waghmare, S. D.; Nadargi, D. Y.; Sartale, S. D.; Kambale, R. C.; Ghodake, U. R.; Suryavanshi, S. S. Magnetic interactions and electrical properties of Tb3+ substituted NiCuZn ferrites. *J. Magn. Magn. Mater.* **2019**, *473*, 99−108.
(45) Harzali, H.; Marzouki, A.; Saida, F.; Megriche, A.; Mgaidi, A. Structural, magnetic and optical properties of nanosized Ni0.4-Cu0.2Zn0.4R0.05Fe1.95O4 (R = Eu3+, Sm3+, Gd3+ and Pr3+) ferrites synthesized by co-precipitation method with ultrasound irradiation. *J. Magn. Magn. Mater.* **2018**, *460*, 89−94.
(46) Kuznetsova, T.; Zubar, T.; Chizhik, S.; Gilewicz, A.; Lupicka, O.; Warcholinski, B. Surface microstructure of Mo(C)N coatings investigated by AFM. *J. Mater. Eng. Perform.* **2016**, *25*, 5450−5459.
(47) Warcholinski, B.; Gilewicz, A.; Kuprin, A. S.; Tolmachova, G. N.; Ovcharenko, V. D.; Kuznetsova, T. A.; Zubar, T. I.; Khudoley, A. L.; Chizhik, S. A. Mechanical properties of Cr-O-N coatings deposited by cathodic arc evaporation. *Vacuum* **2018**, *156*, 97−107.

https://doi.org/10.1021/acsomega.1c00611
ACS Omega 2021, 6, 10266−10280

(48) Warcholinski, B.; Kuznetsova, T. A.; Gilewicz, A.; Zubar, T. I.; Lapitskaya, V. A.; Chizhik, S. A.; Komarov, A. I.; Komarova, V. I.; Kuprin, A. S.; Ovcharenko, V. D.; Goltvyanytsya, V. S. Structural and mechanical properties of Zr-Si-N coatings deposited by arc evaporation at different substrate bias voltages. *J. Mater. Eng. Perform.* **2018**, *27*, 3940−3950.
(49) Lakshman, A.; Subba Rao, P. S. V.; Rao, K. H. Mössbauer spectroscopic analyses of Mg0.9Cu0.1Mn0.05CrxFe1.95−xO4 spinel ferrites. *Mater. Lett.* **2006**, *60*, 7−10.
(50) Almessiere, M. A.; Slimani, Y.; Unal, B.; Zubar, T. I.; Sadaqat, A.; Trukhanov, A. V.; Baykal, A. Microstructure, dielectric and microwave features of [Ni0.4Cu0.2Zn0.4](Fe2−Tb)O4 (x≤ 0.1) nanospinel ferrites. *J. Mater. Res. Technol.* **2020**, *9*, 10608−10623.
(51) Kumar, H.; Srivastava, R. C.; Pal Singh, J.; Negi, P.; Agrawal, H. M.; Das, D.; Hwa Chae, K. Structural and magnetic study of dysprosium substituted cobalt ferrite nanoparticles. *J. Magn. Magn. Mater.* **2016**, *401*, 16−21.
(52) Zhang, Y.; Wen, D. Structural and magnetic study of dysprosium substituted cobalt ferrite nanoparticles. *Mater. Chem. Phys.* **2012**, *131*, 575−580.
(53) Amiri, S.; Shokrollahi, H. Magnetic and structural properties of RE doped Co-ferrite (REåNd, Eu, and Gd) nano-particles synthesized by co-precipitation. *J. Magn. Magn. Mater.* **2013**, *345*, 18−23.
(54) Matzui, Yu. L.; Trukhanov, A. V.; Yakovenko, O. S.; Vovchenko, L. L.; Zagorodnii, V. V.; Oliynyk, V. V.; Borovoy, M. O.; Trukhanova, E. L.; Astapovich, K. A.; Karpinsky, D. V.; Trukhanov, S. V. Functional magnetic composites based on hexaferrites: correlation of the composition, magnetic and high-frequency properties. *Nanomaterials* **2019**, *9*, 1720−1817.
(55) Thakur, S.; Katyal, S. C.; Singh, M. Structural and magnetic properties of nano nickel-zinc ferrite synthesized by reverse micelle technique. *J. Magn. Magn. Mater.* **2009**, *321*, 1−7.
(56) Shirsath, S. E.; Toksha, B. G.; Kadam, R. H.; Patange, S. M.; Mane, D. R.; Jangam, G. S.; Ghasemi, A. Doping effect of Mn2+ on the magnetic behavior in Ni-Zn ferrite nanoparticles prepared by sol-gel auto-combustion. *J. Phys. Chem. Solids* **2010**, *71*, 1669−1675.
(57) Herbst, J. F.; Pinkerton, F. E. Law of approach to saturation for polycrystalline ferromagnets: Remanent initial state. *Phys. Rev. B* **1998**, *57*, 10733−10739.
(58) Topkaya, R. Effect of composition and temperature on the magnetic properties of BaBixLaxFe(12-2x)O19 (0.0 ≤ x ≤ 0.2) hexaferrites. *Appl. Phys. A* **2017**, *123*, 488.
(59) Chikazumi, S. *Physics of Ferromagnetism*, 2nd ed.; Oxford University Press: Oxford, 1997.
(60) Brown, W. F. The effect of dislocations on magnetization near saturation. *Phys. Rev.* **1941**, *60*, 139−147.
(61) Lima, A. C.; Morales, M. A.; Araújo, J. H.; Soares, J. M.; Melo, D. M. A.; Carriço, A. S. Evaluation of (BH)max and magnetic anisotropy of cobalt ferrite nanoparticles synthesized in gelatin. *Ceram. Int.* **2015**, *41*, 11804−11809.
(62) Franco, A.; Machado, F. L. A.; Zapf, V. S. Magnetic properties of nanoparticles of cobalt ferrite at high magnetic field. *J. Appl. Phys.* **2011**, *110*, 053913.
(63) Kubiak, J.; Pietrzak, J. Magnetocrystalline anisotropy of cubic copper ferrite. *Phys. Status Solidi A* **1981**, *67*, 103−108.
(64) Ranvah, N.; Melikhov, Y.; Jiles, D. C.; Snyder, J. E.; Moses, A. J.; Williams, P. I.; Song, S. H. Temperature dependence of magnetic anisotropy of Ga-substituted cobalt ferrite. *J. Appl. Phys.* **2008**, *103*, 07E506.
(65) Kumar, L.; Kar, M. Influence of Al3+ion concentration on the crystal structure and magnetic anisotropy of nanocrystalline spinel cobalt ferrite. *J. Magn. Magn. Mater.* **2011**, *323*, 2042−2048.
(66) de Biasi, R. S.; Cardoso, L. H. G. A simple model for the magnetocrystalline anisotropy in mixed ferrite nanoparticles. *Phys. B* **2012**, *407*, 3893−3896.
(67) Troyanchuk, I. O.; Trukhanov, S. V.; Khalyavin, D. D.; Szymczak, H. Magnetic properties of anion deficit manganites Ln0.55Ba0.45MnO3−γ (Ln=La, Nd, Sm, Gd, γ≤0.37). *J. Magn. Magn. Mater.* **2000**, *208*, 217−220.
(68) Trukhanov, S. V.; Kasper, N. V.; Troyanchuk, I. O.; Tovar, M.; Szymczak, H.; Bärner, K. Evolution of magnetic state in the La1−xCaxMnO3−γ (x=0.30, 0.50) manganites depending on the oxygen content. *J. Solid State Chem.* **2002**, *169*, 85−95.
(69) Lazarević, Z. Ž.; Jovalekić, Č.; Sekulić, D. L.; Milutinović, A.; Baloš, S.; Slankamenac, M.; Romčević, N. Ž. Structural, electrical and dielectric properties of spinel nickel ferrite prepared by sof mechanochemical synthesis. *Mater. Res. Bull.* **2013**, *48*, 4368−4378.
(70) Dimri, M. C.; Kashyap, S. C.; Dube, D. C.; Mohanta, S. K. Complex permittivity and permeability of Co-substituted NiCuZn ferrite at rf and microwave frequencies. *J. Electroceram.* **2006**, *16*, 331−335.
(71) Ponpandian, N.; Balaya, P.; Narayanasamy, A. Electrical conductivity and dielectric behaviour of nanocrystalline NiFe2O4spinel. *J. Phys.: Condens. Matter* **2002**, *14*, 3221−3237.
(72) Abdullah, M. H.; Yusoff, A. N. Complex impedance and dielectric properties of an Mg—Zn ferrite. *J. Alloys Compd.* **1996**, *233*, 129−135.
(73) Wagner, K. W. Erklärung der dielektrischen Nachwirkungsvorgänge auf Grund Maxwellscher Vorstellungen. *Arch. Elektrotech.* **1914**, *2*, 371−387.
(74) Nicolson, A. M.; Ross, G. F. Measurement of the intrinsic properties of materials by time-domain techniques. *IEEE Trans. Instrum. Meas.* **1970**, *19*, 377−382.
(75) Almessiere, M. A.; Trukhanov, A. V.; Khan, F. A.; Slimani, Y.; Tashkandi, N.; Turchenko, V. A.; Zubar, T. I.; Tishkevich, D. I.; Trukhanov, S. V.; Panina, L. V.; Baykal, A. Correlation between microstructure parameters and anti-cancer activity of the [Mn0.5Zn0.5](EuxNdxFe2-2x)O4 nanoferrites produced by modified sol-gel and ultrasonic methods. *Ceram. Int.* **2020**, *46*, 7346−7354.
(76) Almessiere, M. A.; Slimani, Y.; Güngüneş, H.; Kostishyn, V. G.; Trukhanov, S. V.; Trukhanov, A. V.; Baykal, A. Impact of Eu^{3+} ion substitution on structural, magnetic and microwave traits of Ni−Cu−Zn spinel ferrites. *Ceram. Int.* **2020**, *46*, 11124−11131.

https://doi.org/10.1021/acsomega.1c00611
ACS Omega 2021, 6, 10266−10280